JOURNAL OF THE ROYAL SOCIETY Interface

rsif.royalsocietypublishing.org

Review

**Cite this article:** Vielreicher M, Schürmann S, Detsch R, Schmidt MA, Buttgereit A, Boccaccini A, Friedrich O. 2013 Taking a deep look: modern microscopy technologies to optimize the design and functionality of biocompatible scaffolds for tissue engineering in regenerative medicine. J R Soc Interface 10: 20130263. http://dx.doi.org/10.1098/rsif.2013.0263

Received: 21 March 2013
Accepted: 24 June 2013

**Subject Areas:**
biomedical engineering, biomaterials, biophysics

**Keywords:**
multiphoton imaging, second harmonic generation, autofluorescence, biomaterials, artificial tissues, extracellular matrix

**Author for correspondence:**
M. Vielreicher
e-mail: martin.vielreicher@mbt.uni-erlangen.de

Electronic supplementary material is available at http://dx.doi.org/10.1098/rsif.2013.0263 or via http://rsif.royalsocietypublishing.org.

Royal Society Publishing
Informing the science of the future

# Taking a deep look: modern microscopy technologies to optimize the design and functionality of biocompatible scaffolds for tissue engineering in regenerative medicine

M. Vielreicher[1], S. Schürmann[1], R. Detsch[2], M. A. Schmidt[1,2], A. Buttgereit[1], A. Boccaccini[2] and O. Friedrich[1]

[1]Department of Chemical and Biological Engineering, Institute of Medical Biotechnology, Friedrich-Alexander-University Erlangen-Nuremberg, Paul-Gordan-Strasse 3, 91052 Erlangen, Germany
[2]Department of Materials Science and Engineering, Institute of Biomaterials (WW7), Friedrich-Alexander-University Erlangen-Nuremberg, Cauerstrasse 6, 91058 Erlangen, Germany

This review focuses on modern nonlinear optical microscopy (NLOM) methods that are increasingly being used in the field of tissue engineering (TE) to image tissue non-invasively and without labelling in depths unreached by conventional microscopy techniques. With NLOM techniques, biomaterial matrices, cultured cells and their produced extracellular matrix may be visualized with high resolution. After introducing classical imaging methodologies such as μCT, MRI, optical coherence tomography, electron microscopy and conventional microscopy two-photon fluorescence (2-PF) and second harmonic generation (SHG) imaging are described in detail (principle, power, limitations) together with their most widely used TE applications. Besides our own cell encapsulation, cell printing and collagen scaffolding systems and their NLOM imaging the most current research articles will be reviewed. These cover imaging of autofluorescence and fluorescence-labelled tissue and biomaterial structures, SHG-based quantitative morphometry of collagen I and other proteins, imaging of vascularization and online monitoring techniques in TE. Finally, some insight is given into state-of-the-art three-photon-based imaging methods (e.g. coherent anti-Stokes Raman scattering, third harmonic generation). This review provides an overview of the powerful and constantly evolving field of multiphoton microscopy, which is a powerful and indispensable tool for the development of artificial tissues in regenerative medicine and which is likely to gain importance also as a means for general diagnostic medical imaging.

## 1. Introduction

Tissue engineering (TE) has become an emerging field for regenerative medicine, and bringing together patient cells and biocompatible artificial scaffolds for the production of matrix and subsequent revascularization has been often coined as 'the holy grail' on the path to tissue repair and personalized medicine [1]. The cell-centric approach of seeding cells onto a supportive scaffolding material has by far been the most broadly investigated attempt to reconstruct tissues or repair rather smaller defects [2,3].

One major constraint of this approach, however, has been the creation of artificial organotropic environments within small-scale bioreactors to promote cell proliferation into a simplified organomimetic construct, yet largely without vascularization or the complex cellular–matrix coupling usually found within the body [4]. To promote an adequate microenvironment, not only is the continuous development of more biocompatible scaffold compositions a

key requisite, but also the provision of more extended scaffold architectures and designs to account for the three-dimensional aspect of cell seeding and proliferation [5]. In the human body, the extracellular matrix (ECM) and its characteristic cytokine and growth factor profiles may change during spread of precursor cells. These chemical and physical microenvironments may alter the signalling behaviour of ingrowing cells to steer their maturation and differentiation potency [6–8]. This seems to play an important role not only during the early differentiation phase of organogenesis, but may also serve as a reprimable programme during wound healing later in life [9,10]. Other, more unconventional recent TE approaches, suggest omitting the retrieval of source cells for external seeding and aim to use the patient's own cells and cytokine environment to populate an implanted external scaffold [11]. In any case, the structural requirements towards the implemented scaffolds regarding biocompatibility, durability, 'homing suitability', cellular attractibility and mechanical resistance need to be met and are constantly being improved. On the other hand, it is likewise important to confer reliable parameters for the cell–scaffold interaction, desirably online and for extended time periods.

Microscopy technologies probably represent the most adequate means to fulfil such criteria, with light microscopy even having the advantage of not interfering with the biological sample (cells and scaffolds) for a wide range of wavelengths and illumination intensities. Our knowledge of biomaterials, their composition and interaction has evolved tremendously from the application of modern microscopy techniques. One major constraint when it comes to imaging scaffolds and cells seeded within, is the limited penetration depth for most microscopy techniques. Laser confocal microscopy or transillumination microscopy to study the cell–scaffold interfaces or to count cells or follow their trajectory during scaffold population require the use of thin samples or suffer from spatial resolution, respectively.

Multiphoton microscopy (MPM) has overcome most of those constraints and allows imaging deep into the scaffolds, for example, with slicewise optical sectioning and three-dimensional reconstruction, to study the vertical migration or seeding of lacunae within scaffolds with respect to an extended cytomatrix architecture. For MPM, even some specialized optical effects can be used to enable label-free imaging of cells within scaffolds for the least manipulation of the preparation [12,13]. Such novel optical technologies are most promising to study and optimize TE strategies both *ex vivo* and *in vivo*.

This review will provide a state-of-the-art overview of current developments at the interface of regenerative medicine and optical metrology. We give an overview of the recent advances in optical technologies that have been implemented in TE as a novel tool to study cell–matrix architecture of the living preparation. We also give a comparison of multiphoton imaging with other conventional microscopy techniques and highlight their respective advantages and disadvantages. Finally, we present some applications of MPM from our laboratories using examples from Bioglass materials and alginate-encapsulated cells and scaffolds that have been fabricated with tissue plotter technologies. With such novel approaches, we give an outlook on putative future directions that might have a vast impact on the field of TE and regenerative medicine.

## 2. Imaging techniques in the scaffold design and development

During the development of functional tissue constructs, four factors need to be controlled:

— *Cells*. Cell number, viability, growth, morphology, differentiation, cell–matrix interactions.
— *ECM proteins*. Composition, amount, fibre size and spatial orientation.
— *Scaffold*. Surface topography, inner structure, nanoparticle distribution in composites.
— *Post-implantation processes*. Tissue integration, biomaterial degradation and vascularization.

In order to develop custom-tailored and optimized functional tissue implants, a number of techniques are required to both monitor the biomaterial backbone and the cell and tissue behaviour before and after implantation [14].

Scaffold transparency is a major issue in the imaging of TE constructs [5]. Most scaffolds possess a high degree of opacity that could derive from high porosities (e.g. fabrication by particulate leaching or gas foaming), multiple internal surfaces (multi-layered or multi-surface architectures), incorporation of micro- and nanoparticles (nanocomposites) or highly diffracting components such as in biopolymer-based hydrogels. Some scaffolds become highly opaque as a result of increasing mineralization during maturation (bone TE constructs [15]). Light in the UV and visible range (300–700 nm) used for microscopy imaging penetrates such opaque materials only superficially [16] and seeded cells further enhance light diffraction. Because of this, traditional imaging methods relied on physical sectioning (histology) to enable images of the inner micro-architecture, thereby destroying the constructs. Some methodologies, however, overcome this procedure by enabling optical sectioning and three-dimensional reconstruction.

In this section, the most important two- and three-dimensional imaging modalities used in scaffold design and development are discussed. Each one of these methods has its strengths and limitations and allows imaging within certain spatio-temporal boundaries. The techniques differ largely not only in their invasiveness to the biological material, their imaging speed and ability to create three-dimensional views, their biological specificity, imaging depth and resolution, but also in terms of costs and time and effort (table 1).

### 2.1. Tomography methods: μCT, MRI and optical coherence tomography

Useful imaging methods derived from medical diagnostics are tomography-based techniques, the most prominent being computer tomography (CT) and magnetic resonance imaging (MRI) and optical coherence tomography (OCT). These techniques have proved to be powerful in the validation of TE scaffolds [20]. Common to these methods is their ability to scan larger objects, to represent them in three-dimensional and—compared with other available techniques—greatly enhanced imaging depth.

CT and MRI are complementary techniques. In CT, X-ray images are taken from all angles and rendered to three-dimensional volumes. In comparison with MRI, CT has

**Table 1.** Imaging methods used in TE. Physical principle and wavelength range of tissue imaging techniques are stated and methods are compared in terms of their tissue penetration (imaging depth), lateral and axial resolution and other important aspects with ratings from very low/bad (↓↓), low/bad (↓), medium (↔), high/good (↑) to very high/good (↑↑). Invasiveness means destructiveness to tissues and cells. Time and effort means time and work-consumption as well as costs (↑ means that the technique is good in this respect). Additional comments are given for each technique. WL, wavelength; MRI, magnetic resonance imaging; μCT, micro-computed tomography; OCT, optical coherence tomography; LM, light microscopy; CFM, confocal fluorescence microscopy; NLOM, nonlinear optical microscopy; 1-/2-PF, 1-/2-photon fluorescence; SHG, second harmonic generation; CARS, coherent anti-Stokes Raman scattering; EM, electron microscopy; ET, electron tomography; n.a. not applicable.

| method | physical principle | WL range | imaging depth | lateral resolution | axial resolution | three-dimensional imaging | acquisition speed | invasiveness | specificity | time and effort | comments | reference |
|---|---|---|---|---|---|---|---|---|---|---|---|---|
| MRI/μCT | NMR/X-ray diffraction | radio frequency/X-rays | whole body | approximately 100 μm/>1 μm | approximately 100 μm | ↑↑/↑↑ | ↓/↔ | ↑/↓ | ↔/↔ | ↓↓/ ↓↓ | low biological specificity<br>MRI: low resolution and speed, applicable for soft tissue imaging<br>μCT: medium resolution, preferentially used for hard tissue imaging | [17–21] |
| OCT | low coherence interferometry | NIR (800–1300 nm) | <2 mm | 3–4 μm | >10 μm | ↑↑ | ↑ | ↔ | ↑ | ↓ | owing to limited resolution only indirect cell imaging possible | [22–24] |
| LM | light diffraction and interference | Vis (380–760 nm) | n.a. | 200–350 nm | n.a. | ↓ | ↑↑ | ↑ | ↔ | ↑ | very easy, cheap and fast method, but low specificity (if used without staining) | [25,26] |
| CFM | fluorescence (1-PF) | UV/Vis (340–780 nm) | <100 μm | 200–500 nm | 500–1000 nm | ↑↑ | ↑ | ↓ | ↑↑ | ↔ | bleaching, low imaging depth and signal intensity, stainings required. Increase in resolution and speed possible with STED, 4Pi and spinning disc techniques | [25–28] |
| SEM/TEM/ET | electron diffraction | approximately 100.000× shorter than visible light | n.a./ <200 nm/ <200 nm | 1–5 nm/>0.2 nm/ 5–20 nm | n.a. | ↓↓ | ↓↓ | ↓↓ | ↑↑ | ↓↓ | sample destruction, artefacts, time-consuming (histology)<br>ET: three-dimensional imaging possible | [28–30] |
| NLOM | 2-PF/SHG/CARS | NIR | usually <1000 μm | 200–500 nm | approximately 1400 nm | ↑↑ | ↑ | ↑ | ↑↑ | ↓ | 2-PF: thermal damage, accelerated bleaching in the focal point<br>SHG: limited to selected molecules | [27,31–38] |

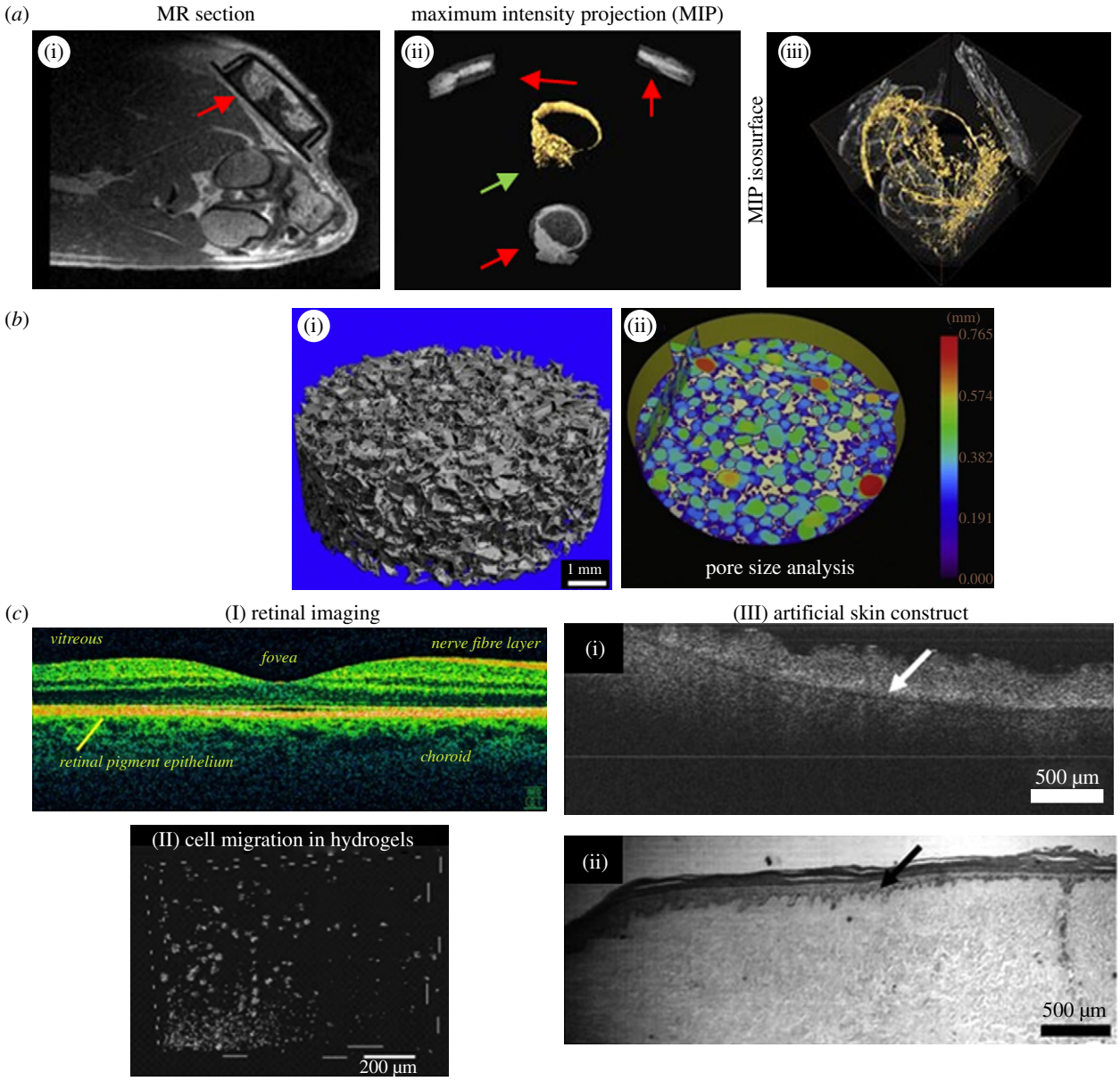


**Figure 1.** MRI, µCT and OCT imaging. (*a*) MRI and µCT for the detection of neovascularization. (i) MRI angiography of an implantation site showing an isolation chamber (red arrow, height 1.2 cm) containing an arteriovenous loop, four weeks after implantation. (ii) Loop region from three spatial directions (red arrows, MIP: maximum intensity projection). Three-dimensional image of the loop (yellow) showing the blood vessels (green arrow). (iii) Three-dimensional display the explanted and perfusion-treated loop imaged with µCT. Number and total length of newly formed vessels can be determined [39]. (*b*) Use of µCT for scaffold characterization. (i) Detailed µCT three-dimensional image of a poly-(D,L)-lactate scaffold containing 10% Bioglass. (ii) Colour-coded scaffold micro-architecture: The intermeshing, overlapping colour circles, i.e. colour-coded pores (200–750 µm) indicate high pore interconnectivity and high porosity [40]. (*c*) OCT. (I) *In vivo* OCT scan of a human retina using 800 nm illumination light. The high axial resolution (3 µm) allows differentiation of the various cell layers and detection of structural aberrations (e.g. in multiple sclerosis) [41]. (II) Three-dimensional OCT image demonstrating the migration of macrophages through Matrigel-coated porous membranes [42]. (III) Comparison of an OCT image (i) with photomicrographs of H&E-stained histological sections (ii) of engineered skin based on de-epithelialized acellular dermis. Non-invasive OCT resolves the same amount of detail as histology at the given optical resolution. Arrows indicate the boundary between the dermal component and the epidermis [43].

much better lateral resolution (approx. 1 versus 100 µm) [17], and scan times and image generation are much faster, but it requires contrast agents and uses ionizing radiation. CT is, in general, stronger in hard-tissue imaging (bone, teeth or cartilage), but it can also be applied to study vascularization (figure 1*a*). Micro-CT (µCT), a small-scale CT application, is commonly used to study scaffold structures (figure 1*b*). The X-rays used show a high degree of scaffold penetration. Interesting aspects to be studied are, for example, porosity and pore interconnectivity, both of which are essential for cellular penetration, vascularization, tissue in-growth and waste removal and oxygen and nutrient delivery within a cell-seeded scaffold. The technique was further used for determining pore size distribution of PDLLA–Bioglass composites and other scaffolds and in studies of collagen, Bioglass and mineral phases in bone mimetic scaffolds [44–48].

MRI has been used in radiology to visualize internal structures of the body in detail. It uses nuclear magnetic resonance (NMR) to differentially image the distribution of water molecules in various tissues by applying strong magnetic fields. This non-invasive technique is able to scan large volumes (organ up to whole-body scans), but it requires additional manual editing of images [20]. MRI provides very good contrast between the different soft tissues [21] which renders it especially useful in imaging brain, muscles, heart, vascularization or cancer. In TE, MRI has been applied for

studying bone, cartilage or adipose tissue [17], scaffold structures and implanted tissue grafts [49–51]. Boos *et al.* [39] have used both MRI and CT to image newly formed bone in an arteriovenous loop model in order to assess the volume of neovascularization (figure 1*a*(i–ii)). The major drawback of both CT and MRI is relatively low resolution (fail to resolve single cells), which limits their biological significance [20].

Another tomography method, OCT, is increasingly being used in imaging of engineered tissue [52]. OCT is an interferometry technique using broadband near-infrared (NIR) light beyond 800 nm. It enables non-invasive and label-free real-time three-dimensional imaging [22,53,54] and relatively deep penetration into tissues (up to 2000 µm) compared with other visible or NIR light techniques ([39]; table 1). In relation to MRI and µCT, penetration is low; however, what makes OCT strong is that it resolves structures almost at the cellular range. OCT has been applied in the detection of structural changes of the retina (figure 1*c*(I)) or skin cancer, for instance. Two techniques can be differentiated, structural and functional OCT. Structural OCT has been used to investigate how engineered tissue morphology and cell populations change over time, whereas functional OCT techniques were rather used to extract information related to tissue elasticity, fluorescence and spectroscopic properties [23]. Some studies applied OCT for three-dimensional characterization of polylactate and chitosan scaffolds. In other research work, cell behaviour, kinetics of cell invasion into collagen gels and three-dimensional cell models were studied with OCT (figure 1*c*(II)) [25,53,54]. By observing the calcification process in the gelatine gels, OCT proved useful to mimic bone regeneration [23,42,49,55–57]. OCT has also been used to study the cellular growth within TE constructs and three-dimensional tissue models, including skin models (figure 1*c*(III)) [25,43]. Optical coherence tomography is strong in terms of imaging speed (250 megavoxels $s^{-1}$), axial resolution (less than 0.5 µm) and non-invasiveness, which is ideal for long-term studies [58,59]. Limitations of the technique are low lateral resolution (typically 5–10 µm), which makes it difficult to resolve individual cells. However, as the technique has great potential to be developed further (resolution, imaging speed, penetration depth), OCT will become a powerful complementary technology to MPM [23].

## 2.2. Transillumination and fluorescence microscopy

The most traditional tool to image cells and tissues is optical microscopy, with a large number of techniques available. Common to these techniques is their resolution window which is determined by the wavelength of the illumination light. Light microscopes use a transmitted white light spectrum for image generation. As a versatile, fast and affordable imaging tool, white light microscopy is frequently used in TE. Besides basic bright-field illumination [36,60], enhanced contrast methods such as dark-field illumination, phase-contrast and differential interference contrast techniques have been applied [61–64]. White light microscopy is primarily used for routine analysis (monitoring cell number and morphology after seeding of scaffolds) and for imaging stained tissue slices (histology [65]; various stains such as H&E, Von Kossa, trichrome, alcian blue and others are available [39,50,66–71]). A typical study that makes use of histology was carried out by Gerhardt *et al.* [40], who investigated scaffolds after explanation to observe their degradation, cellular infiltration and vascularization (figure 2*a*). The limitations of white light microscopy are low contrast and low specificity in unstained samples. Opaque scaffolds cannot be examined with transillumination microscopy.

In fluorescence microscopy (FM), a sample is illuminated by light in the near UV or lower visible spectrum to excite fluorophores within the sample. These are either extrinsically applied or intrinsically present as autofluorescent molecules. The fluorophores are detected on the basis of their fluorescence excitation and emission capabilities. The emission light has a larger wavelength (lower energy) than the excitation light (Stokes shift) and is separated and collected by appropriate beam splitters, dichroic mirrors and emission filters. Unspecific background owing to cellular autofluorescence is an important problem that needs to be controlled. A huge increase in image contrast is gained by the use of laser scanning confocal fluorescence microscopy (CFM) [25,26]. CFM uses point illumination and optical sectioning by applying an adjustable pinhole in the emission light path which lets only fluorescence from a defined *z*-plane pass through and excludes any out-of-focus light [81]. The reduced light intensity is overcome by sensitive photomultiplier detectors. CFM enables reconstruction of three-dimensional structures from the obtained image stacks [82,83]. The major concern about CFM is the issue of photobleaching and phototoxic effects to cells (invasiveness) owing to high laser intensities in the focal plane and ever present out-of-focus excitation (figure 3*b*,*c*) which complicates long-term imaging. The other major limitation is low tissue penetration of only around 100 µm [25,27,84]. Therefore, bright and photostable dyes (e.g. Alexa Fluor, Cy, MFP or Qdot series) are used in many TE studies [85–88]. CFM is used to stain both fixed and live cells with nuclear, cytoplasmic, membrane-bound dyes or—for protein-specific detection—antibody-coupled dyes [59,64,65,68,69,76] (immunohistochemistry: [39,89]). In principle, any cellular structure can nowadays be specifically visualized and combinations of dyes are possible (multicolour imaging, multiplexing) when spectral overlap is minimal between dyes. To overcome the artificial exogenous staining of tissues, genetically encoded fluorescent proteins (GFP variants) can be expressed [90,91]. FM and CFM are powerful tools that are used to get an overview of cell distribution and cell morphology (spreading, surface coverage) of scaffold-seeded cells (figure 2*b*) [44], to test for the presence of marker proteins or in cell viability testing with two-colour stains (calcein and EthD-III) to determine the percentage of dead cells. Another application where CFM is useful is imaging and modelling of collagen gel networks [82,92].

## 2.3. Electron microscopy

It has been recognized that for the success of TE knowledge of nanostructures at the scaffold, cell and ECM level is required. For example, the critical factor of cell seeding onto a scaffold is—besides the selected biomaterial—the surface topography (e.g. roughness), pore size distribution and interconnectivity and architecture of included nanofibres and nanoparticles. Owing to its extremely high resolution, electron microscopy (EM) has the power to resolve such nanostructures in detail. In EM, electrons are accelerated within an ultra-high vacuum (to variable energy, determining resolution power) and focused onto the specimen that needs to be stained with electron diffracting atoms.

Two EM methods are distinguished, scanning and transmission electron microscopy (SEM and TEM). SEM uses

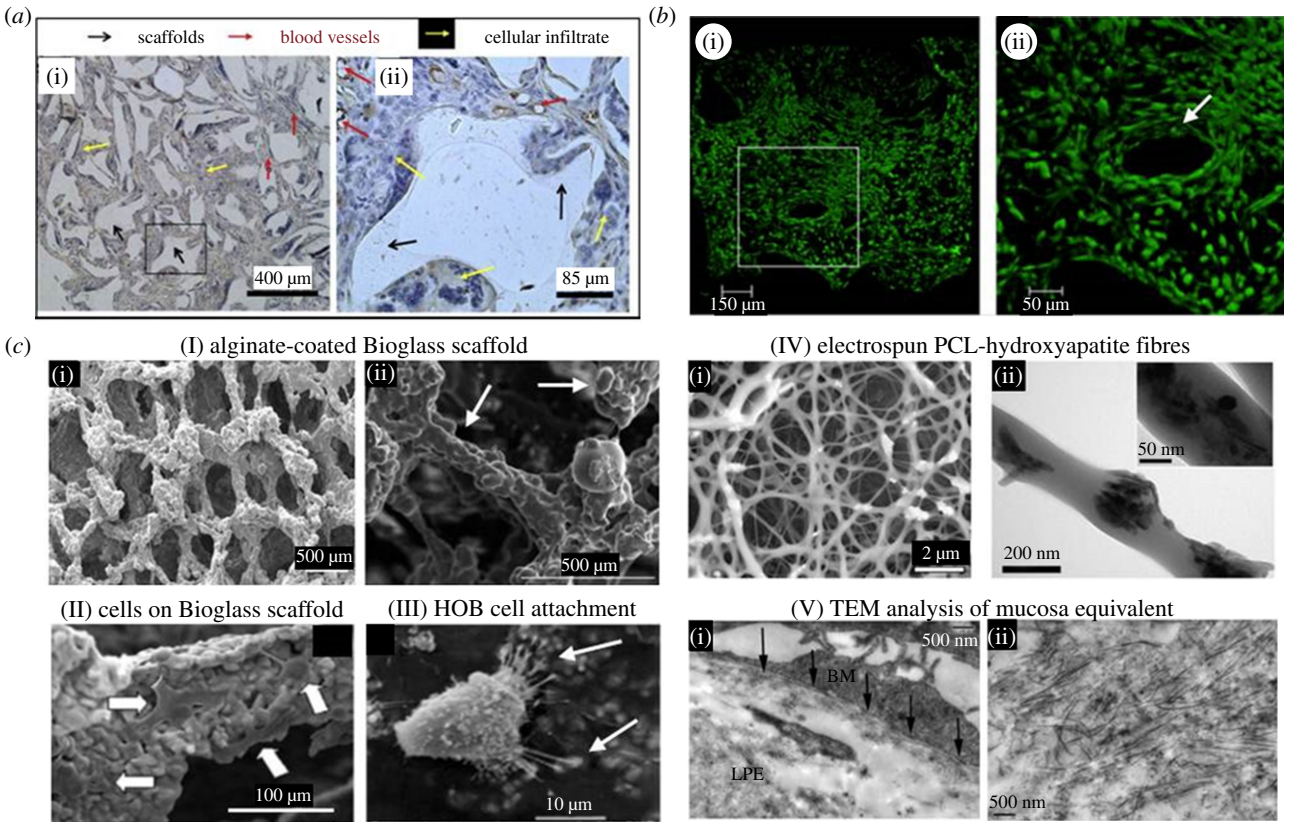


**Figure 2.** White light, fluorescence and electron microscopy applications in TE. (*a*) White light images of tissue slices after histological staining. Image of a post-implantation poly-DL-lactate (PDLL) scaffold after eight weeks, stained with haematoxylin and an antibody against Factor VIII (brown rings) in (i) low and (ii) high magnification (area marked in (i)). The scaffold was well interspersed with tissue and blood vessels. Key: black arrows: scaffold (opaque material), red arrows: blood vessels, immuno-localized for factor VIII, yellow arrow: cellular infiltrate [40]. (*b*) Three-dimensional confocal fluorescence imaging of a bone TE scaffold. GFP-labelled MSCs seeded on hydroxylapatite (HA) ceramics were imaged at day 7 and analysed for cell polarization and migration into the scaffold ((i) low, (ii) high magnification of squared region in (i)). The scaffold surface is covered with cells deep into single pores which remain open (ii, white arrow). Polarized cells surrounding the pores give an impression of the inter-connective pore system [71]. (*c*) SEM and TEM. (I) Bioactive glass scaffolds with uniform alginate-coating (white arrows in (ii); (i) low, (ii) high magnification SEM images [78]. (II) Attachment of MSCs (white arrows) to the pore walls of a Bioglass scaffold after two weeks of culture shown with SEM [79]. (III) SEM image from primary human osteoblast-like (HOB) cells on poly-methylmethacrylate (PMMA)/nano-HA scaffold showing normal osteoblast morphology and attachment to the HA crystals at the scaffolds surface [80]. (IV) EM images of a PCL (poly-caprolactone)/nanosized HA particles electrospun fibrous scaffold. (i) SEM image, (ii) TEM image of a single fibre with attached HA crystals [75]. (V) Ultra-structural TEM analysis of a human oral mucosal equivalent. In (i), the basement membrane anchors the epithelium firmly to the lamina propria equivalent (LPE) below (black arrows). (ii) Newly synthesized collagen I fibrils within the LPE [67].

raster scanning which provides signals carrying information about the properties of the specimen surface and its three-dimensional shape. In order to get a conductive layer, the samples need to be treated with heavy atoms (gold, platinum or osmium). SEM has frequently been used to characterize the micro- and nanostructure of scaffolds. For example, Erol *et al.* [78] have produced sintered Bioglass scaffolds (suitable for bone TE) with an average pore size of 325 µm and a pore size distribution ranging from 110 to 550 µm and also characterized the scaffolds surface (figure 2*c*(I)). Likewise, efficiency of cellular seeding, cell distribution and orientation down to cell adhesion structures can be imaged in order to evaluate the scaffold quality (figure 2*c*(II,III)). Further applications are the analysis of electrospun nanofibres of various organic polymers (PLLA/PLGA), ECM proteins such as collagen or fibrin or studies of fibroblasts seeded on GMMA polymers [93].

TEM offers the highest possible magnification and resolution (approx. 10 times higher than SEM; table 1). Owing to the very low tissue penetration of electrons, TEM requires ultra-thin sample sections (approx. 60–80 nm) to let electrons pass through the specimen to acquire transmission images. Samples need to be fixed, dehydrated and mounted to stabilize them mechanically in order to allow sectioning with an ultra-microtome. Sections of biological specimens require special staining with heavy atom salts (uranyl acetate, lead citrate) to achieve the required image contrast. Polini *et al.* [75] have used TEM for morphometric analyses of fibre diameter and HA nanoparticle size and distribution (figure 2*c*(IV)). TEM was used to study critical tissue sites (such as barrier membranes) or subcellular morphology [94]. Kinikoglu *et al.* [67] analysed human oral mucosa equivalents and imaged the integrity of epithelial cell layers, lamina propria and basement membrane (figure 2*c*(V)). TEM was further used in ultra-structural analysis of carbon nanotube binding to breast cancer cells [95], of bone (nanosized HA crystal structure and interaction with collagen fibres [96]) and in the immunogold applications [97].

However, there are clear disadvantages: a multitude of time-consuming and costly processing steps are required and the possibility of processing artefacts persistently remains. The technique involves the sacrifice of sample viability and for long-term observations large numbers of tissue slices are required. An exception to this is electron tomography (ET), a complex and highly advanced imaging technique. ET was used for

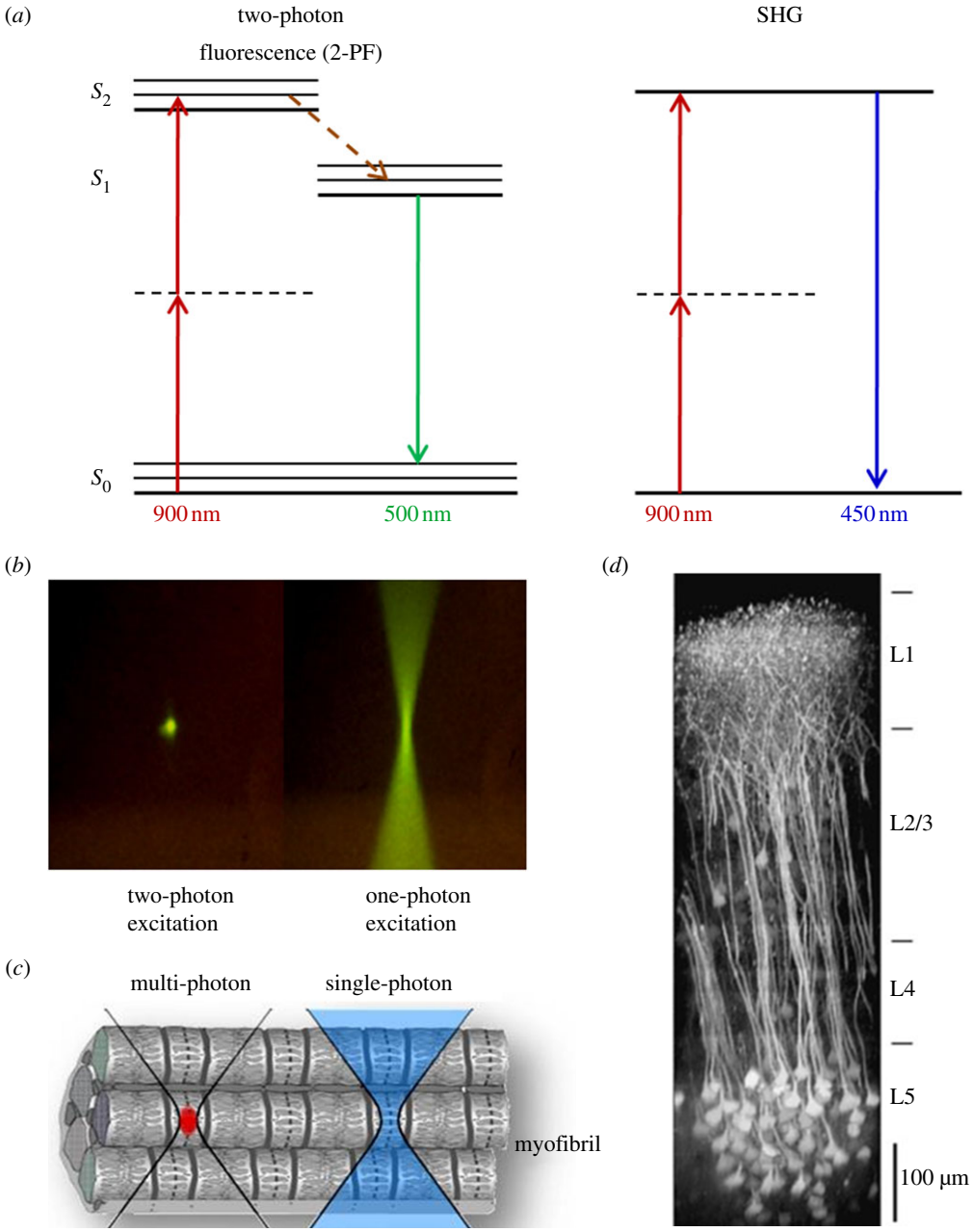


**Figure 3.** Multiphoton microscopy: principle, micrometre-scale excitation and tissue penetration. In (*a*), the principle of 2-PF and SHG is explained, and the Jablonski diagrams show the energy levels involved and the excitation and emission processes. With 2-PF, the excitation does not occur with one photon of 450 nm, but with two near-simultaneous photons of 900 nm (half the energy) each. Owing to certain quantum mechanical selection rules that apply for 2-PF other than 1-PF, in reality, excitation energies are not exactly one-half (emission is unchanged). In SHG, two photons (900 nm) simultaneously striking a highly ordered, non-centrosymmetric material may induce a virtual energy state transition that lasts only as long as the illuminating pulse (approx. 1 fs) and results in rapid relaxation to $S_0$ and the release of a photon of exactly twice the energy of the incoming photons (450 nm). No photons are absorbed, and resonance enhancement of SHG can occur. (*b*) Comparison of two- and one-photon excitation by use of a fluorophore solution. Two-photon excitation generates fluorescence exclusively in the focal volume, whereas in one-photon excitation, fluorescence is generated all along the light path. (*c*) Only with multiphoton fluorescence microscopy, is it possible to excite a confined focal volume (red) within a tissue or even cell. (*d*) Illustration of deep-tissue imaging in the mouse neocortex. A maximum intensity side projection of a fluorescence image stack obtained in a transgenic mouse expressing a genetically encoded indicator is shown. Nearly the entire depth of the neocortex can be imaged [27].

three-dimensional analysis of tissue–biomaterial interfaces and for resolving the ultrastructure of actomyosin linkages and intracellular $Ca^{2+}$ stores within muscle cells [30,98,99].

## 3. Multiphoton imaging and its use in tissue engineering

An advanced optical microscopy technique, which largely overcomes many of the limitations of the aforementioned techniques is MPM (in the following, termed also as nonlinear optical microscopy, NLOM). Nonlinear effects are based on more than one photon interacting with a molecule within an extremely short time-period [27,37]. Signal magnitude does not increase linearly with the number of illuminating photons (such as normal 1-photon fluorescence, 1-PF—in CFM), but with its square (second-order processes, two-photon effect) or third power (third-order process, three-photon effect). NLOM requires very high photon densities of defined wavelength in the focal point of the microscope, whereas outside

the focal volume, photon density rapidly decreases [32]. This means that there is an intrinsic pinhole effect and pinhole size is largely determined by the numerical aperture (NA) of the objective by which photons are focused [100]. Excitation wavelengths used in MPM are two to threefold longer than in 1-PF with the consequence of deeper penetration of tissues with high opacity due to less diffraction. The benefit of confined excitation (only localized bleaching) and deeper tissue penetration applies to all nonlinear optical techniques (figure 3).

Examples for NLOM are applications based on different physical principles such as fluorescence (two- and three-photon excited fluorescence, 2-PF, 3-PF), second and third harmonic generation (SHG, THG) and coherent anti-Stokes Raman scattering (CARS). These imaging techniques allow label-free, minimal- or non-invasive, deep-tissue imaging suitable for long-term investigations. The principal possibility of simultaneous excitation of two or more photons (nonlinear effects) was predicted by Göppert-Mayer [101]. Shortly after the invention of the first lasers, the two-photon effect was experimentally proved [102], but it lasted until pulsed sub-picosecond mode-locked laser systems were developed that the effects could be applied to microscopy [103]. SHG was first used in microscopy to image collagen I without any kind of staining [104] and thus was one of the earliest forms of biological nonlinear microscopy demonstrated. Even earlier, CARS, one of the most complex forms of nonlinear imaging based on the three-photon effect, was developed [105].

In the context of scaffold design and development, imaging methods are required to visualize, test and control the direction in which the scaffold develops, both before and after implantation into the body. NLOM unites a number of beneficial features that enable detailed views into regions deep inside scaffolds and engineered tissues [35]. In this chapter, the most common NLOM techniques will be explained and results from our laboratories and from current TE-related research articles will be presented and discussed.

## 3.1. Technical requirements

In principle, MPMs are specialized laser scanning microscopes. To generate nonlinear optical effects, multiple photons of identical wavelength need to be present at virtually the same time ($10^{-18}$s or 1 as) at the location of electronic excitation. This is only possible with pulsed NIR lasers that generate extremely high photon fluxes ($10^{20}$–$10^{30}$photons cm$^{-2}$ s) [27] during pulsing. The most widely used NIR lasers are mode-locked Ti : Sa lasers (700–1050 nm) with ultra-short pulses (approx. 150 fs) with extremely high energy intensity and high repetition rates of typically 80–100 MHz [32]. The average power of such lasers, however, is comparably low allowing non- or least-invasive biological imaging.

State-of-the-art MPMs use beam shapers to create tailored pulse shapes and wavefronts for optimized excitation. As mentioned, in MPM, excitation wavelength is roughly two to threefold longer than emission. This instance requires optical components with advanced properties. Components such as beam splitters, dichroic mirrors, lenses or objectives need to be widely transmittant in the NIR (excitation part) and eventually UV (emission part). For effective excitation, objectives with high NA are required to focus photons to a confined focal volume (approx. 1 fl or 1 $\mu$m$^3$). MPM also requires highly sensitive non-descanned photomultiplier detectors to maximize photon counts. These detectors are, therefore, located close to the sample and separated by a minimum of optical components to maximize collection efficiency.

An expansion of excitation wavelength range further into the NIR (up to 1300 nm and beyond) is possible using an optical parametric oscillator (OPO), which uses the NIR laser for pumping. The resulting wavelengths allow the imaging of red dyes (2-PF), proteins (via tryptophane fluorescence) and certain UV-excited molecules (3-PF) and THG applications (§3.5). Multifocal MPM is another application that allows high-speed imaging with multiple foci at a time splitting up the primary beam into up to 64 beamlets [31,106,107].

## 3.2. Two-photon fluorescence microscopy

In contrast to CFM, in 2-PF microscopy, two near-simultaneous photons of half the energy (double the wavelength) are required for excitation which is confined other than present all along the light cone of the illuminating light (figure 3*a*,*b*). As shown in a cartoon in figure 3*c*, a single cell within a tissue (here a skeletal muscle myofibril) may be selectively excited using 2-PF. Bleaching and phototoxicity is a major problem in 1-PF, which uses high-energy visible light. In 2-PF and even more so in 3-PF, the energy of NIR photons is much lower causing much less photobleaching outside the focal volume. This less-invasive approach enables engineered tissues to be observed longer without major detriments to overall viability. The 2-PF excitation photons will penetrate tissues easier (around sixfold compared with CFM) due to less diffraction and cause fluorescence at depths of 1000 $\mu$m and deeper depending on tissue transparency. Ustione & Piston [27] visualized structures deep within the mouse neocortex with a side projection reconstructed from fluorescence image stacks (figure 3*d*).

### 3.2.1. Autofluorescence imaging

Cells and tissues contain intrinsic fluorescent molecules excitable in the whole visible light spectrum (e.g. enzymatic co-factors such as NADH and flavins) generating autofluorescence (AF). Compared with fluorescent stains, these fluorophores are much less bright and stable and thus, rapidly bleach out with confocal microscopy producing phototoxicity-caused cell stress. With 2-PF, however, these endogenous molecules can be imaged with high contrast with overall low photobleaching. In figure 4*a*, the most important autofluorescent molecules are listed with large differences in their two-photon excitation efficiency with 700–800 nm being the most effective range for most molecules (i). The corresponding fluorescence shows that there is a large spectral overlap at 400–600 nm (ii). Figure 4*b* demonstrates the power of two-photon AF in tissue imaging [108]. The comparison of MPM images (i, 2-PF) and histology sections (ii) proves that in ovarian tissue, 2-PF delivers an endogenous contrast that is comparable to conventional histology staining. Furthermore, images (iii) and (iv) present some highly contrasted details of extracellular fibrous components. These findings demonstrate that 2-PF is a powerful tool for imaging native tissues.

In TE studies, 2-PF was applied for imaging cellular AF caused by NADH, FAD and other flavoproteins as well as lipofuscin [74,109]. Apart from structures surrounding the nucleus (e.g. mitochondria, lysosomes or ribosomes), very often, the ECM can be imaged as well, for example elastin

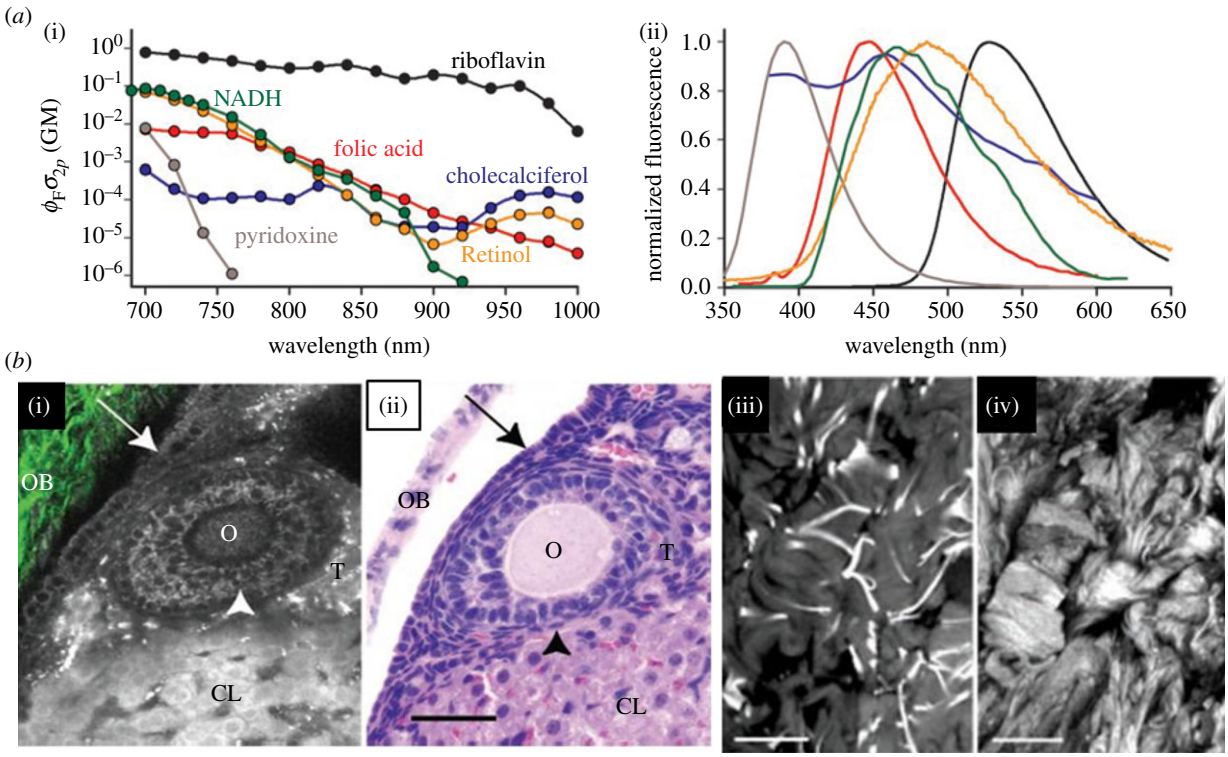


**Figure 4.** Sources of intra- and extracellular autofluorescence. (*a*) Most important intracellular autofluorescent molecules are listed together with their two-photon absorption probability (two-photon action cross-section, (i) and emission spectra (ii)). AF can be excited over a large range of the visible spectrum. (*b*) AF is a suitable tool to visualize important tissue structures. (i) and (ii) show intracellular fluorescence sources: (i) presents an multiphoton image (fluorescence in greyscale, SHG in green-collagen) and (ii) the corresponding H&E-stained histological image of a mouse ovarium. The ovarian epithelium (arrow), oocyte (O), granulosa cells (arrowhead), thecal cells (T), the corpus luteum (CL) and ovarian bursa (OB) are all clearly resolvable and resemble the histological image in (ii). In (iii) and (iv), ECM structures are shown. Image of elastin fibres of a human skin explant ((iii), 740 nm) and SHG image (iv) shows collagen structure taken at 800 nm. Images from Zipfel *et al.* [108].

fibres [63]. In a study by Dittmar *et al.* [110], two-photon AF was used to assess cell viability which is an important parameter in TE to evaluate the effect of environmental conditions on cell behaviour. Live and dead cells could be distinguished spectrally, and viable cells showed predominantly blue fluorescence (peak emission around 470 nm), whereas dead cells appeared to mainly emit green fluorescent light (approx. 560 nm).

Cellular AF imaging using 2-PF is frequently used in TE studies. In our laboratories, we have extensively studied cells in alginate-based hydrogels which represent very promising biocompatible and degradable biomaterials, especially in bone TE (details of all materials and methods used can be found within the electronic supplementary material) [111–114]. An additional compound in hybrid (composite) scaffolds is bioactive glass, especially Bioglass 45S5, which supports bone formation and angiogenesis [115,116]. We have studied cellular autofluorescence in different biomaterial combinations and matrix architectures. Among these encapsulated cells (diameter: 300–600 µm), cells printed in three dimensions and cells grown on two-dimensional hydrogel films have been investigated. The AF images in figure 5*a*(i) show encapsulated cells in pure alginate that were roundish and did not interact with the biomaterial, whereas cells in alginate-RGD (20× image below) were adherent (through the RGD domain) with clearly visible cell edges. In alginate-RGD capsules containing nanosized Bioglass, calcification occurred and cells were induced to undergo osteogenesis (images ii, large non-transparency visible in the transmission image). These results demonstrate that 2-PF AF imaging has the power to resolve cellular details even within highly non-transparent and relatively large capsules. In another three-dimensional cultivation approach, we have produced cell-loaded hydrogel scaffolds of defined geometries with the aim to imitate tissue architectures with cell plotter technologies [117,118]. In our studies, the osteosarcoma cell line MG-63 was embedded in alginate–gelatin blend material and printed in a defined array of strains (diameter: 200 µm, spacing: 600 µm). The transmission image in figure 5*b* depicts a section of one of the scaffolds with cells grown to a large density. The AF images resolve the subcellular localizations of AF signals near the nucleus (likely the endoplasmic reticulum, mitochondria and protein containing vesicles). Both encapsulated and printed cells are protected from environmental stress and can be cultured for extended time periods in non-invasive studies of three-dimensional tissue formation without staining and with almost no bleaching. Close to the pores, the cells have a strongly stretched morphology. Another culturing approach is shown in figure 5*c*. MG-63 cells were grown on alginate–gelatin hydrogel films for four weeks. We used this simplified two-dimensional system to image the formation of ECM fibres. Cellular AF imaging is very easily possible (40× image), but also fibrous structures could be detected above the cell layer (*z*: +10 µm) indicating the production of the ECM (40× image, arrows pointing to fibrous network).

Not only tissue but biomaterials can also be imaged and characterized using two-photon AF. In a study by Chen *et al.* [109], the selected chitosan scaffold material showed strong AF that could be applied for the study of cell–biomaterial

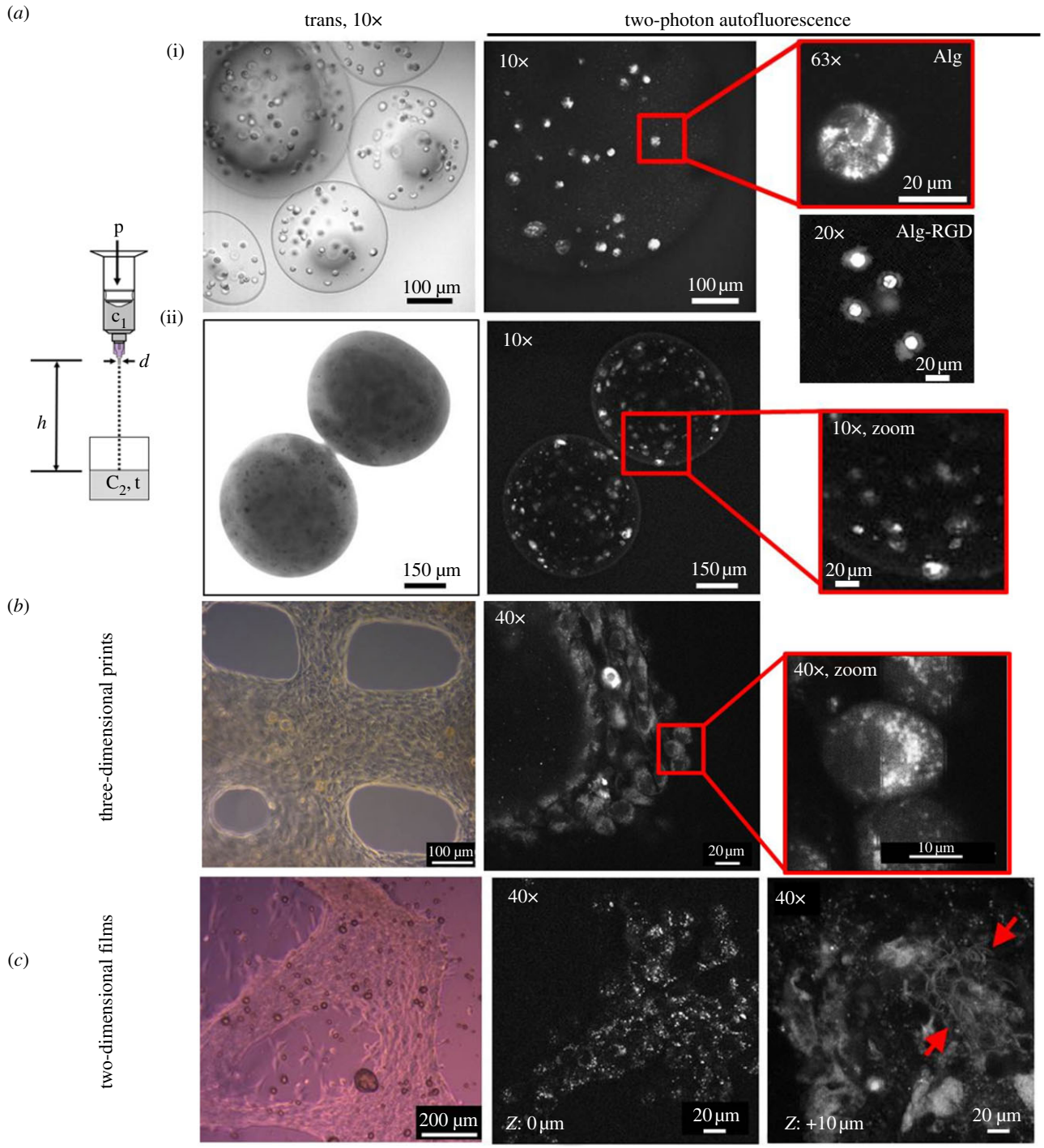


**Figure 5.** Two-photon AF images of cells in different scaffold designs. MG-63 cells grown in different biomaterial combinations and architectures (excitation at 790 nm). (*a*) Hydrogel capsules. The scheme shows the process of droplet formation by pressure-driven extrusion of hydrogel solution from a specially designed syringe. The gelation of alginate occurs with droplet contact with the $CaCl_2$ solution. (i) Cells in alginate (Alg) capsules after two weeks: cells do not attach to alginate. Image (63×) of a rounded cell. The 20× image below shows a cell encapsulated in alginate-RGD (Alg-RGD). Cells spread out, cell edges can be identified. (ii) Cells encapsulated in alginate-RGD/nano-Bioglass after five weeks in culture. Capsules are almost non-transparent; however, 2-PF still allows AF imaging of cell distribution and morphology deep inside the capsule. (*b*) Prints of cells in alginate–gelatin blend hydrogels (80 : 20), cultivated for six weeks. The pores between the gel strands are partially closed due to gel fluidity. Spatial organization of cells with subcellular AF localization is visible (40× zoom). (*c*) Cells on alginate–gelatin blend films (80 : 20) after four weeks in culture. Adherent cells cover wide areas of the surface. Above the cell layer, regions with fibrous structure were detected (ECM fibres).

interactions (described in §3.3.1). Rice *et al.* [119] characterized silk fibroin (in the form of fibres, scaffolds, hydrogels and films) and studied the effect of hydration/dehydration, gelation time and biomechanical treatment (compression and stretching) on the autofluorescence (and SHG) signals. An interesting finding was that AF imaging of the silk scaffold morphology provided comparable information to SEM analysis, which is classically used to study scaffold structures. Other results demonstrated that 2-PF and SHG were highly sensitive to the hydration, overall β-sheet content and to the molecular orientation of the sample. These findings have implications for understanding and tracking the remodelling of degradable biomaterials under dynamic conditions both *in vitro* and *in vivo*. Sun *et al.* [36] imaged a number of scaffolding materials (PGA, open-cell PLA, nylon, Collagraft, collagen scaffold) and spectrally resolved and quantified AF signals in three wavelength-specific channels: a blue (435–485 nm), a green (500–550 nm) and a red (550–630 nm). The materials

produced spectral patterns of signal intensity which were ratiometrically analysed. By this, it was possible to clearly differentiate the biomaterials based solely on their signal intensity distributions.

#### 3.2.2. Imaging of labelled structures

Two-photon fluorescence is also frequently used to image labelled scaffolds and tissues at larger depth. Most dyes excitable with 1-PF can also be applied for 2-PF; however, two-photon cross sections and thus, excitation efficiency may vary strongly. Design of 2-PF dyes is therefore based on appropriate theoretical considerations [120]. Many conventional fluorescent dyes have a much broader and differently shaped excitation spectrum when excited with pulsed NIR lasers instead of visible lasers used in 1-PF excitation (figure 6*a* versus figure 6*b*). As a consequence, spectra of many dyes largely overlap (B). The reasons for these changes are represented in quantum mechanical selection rules that apply for 2-PF other than for 1-PF. While emission spectra mostly look the same between 1-PF and 2-PF, two-photon excitation spectra are shifted more or less towards shorter wavelengths. In figure 6*c*, this effect is demonstrated by a list of frequently used fluorophores.

Fluorescent dyes that have frequently been applied in TE studies are DNA stains (DAPI, Hoechst, propidium iodide, SYTO) [13,122], membrane stains (DiA, DiI, DiO, BODIPY) [38,123] or cytoplasmic stains such as calcein, CellTracker blue or CFDA [85,124,125], but also actin labelling with labelled phalloidin [61,85] as well as organelle markers (MitoTracker for mitochondria or LysoTracker for lysosomes) are widely being used [74]. An interesting approach is the use of fluorescent semiconductor nanocrystals (Qdots or Qtracker) with excellent optical and spectral properties [86]. Qtracker is taken up irrespective of the cell type, shows low cytotoxicity, remains inside the cells for extended time periods and is detectable even in very low concentrations. After loading Qtracker into the cells [126], cell migration can easily be tracked with 2-PF [127]. An important advantage over conventional labels is that Qdots greatly simplify multicolour experiments, because different Qdot types can be excited with a single wavelength and their emission wavelengths are related to the diameter of the semiconductor crystal [128,129].

Staining of encapsulated cells with conventional fluorescent dyes such as DAPI (nuclear stain) or calcein (cytoplasmic stain) has been performed in our laboratories using 2-PF (figure 6*d*). This dye combination is frequently used for live–dead cell screening (DAPI stains dead, calcein live cells). In figure 6*d–i*, alginate-RGD-encapsulated and DAPI-stained cells are shown together with a three-dimensional reconstruction image from a stack of 30 images. This allows the determination of the number and three-dimensional distribution of dead cells within the capsules. High-resolution reconstructions are possible with very low *z*-interlacing distances (e.g. 0.3 µm). Owing to their spectral separation, DAPI/calcein double-stained cells are simultaneously excited at 1000 nm (2-PF of calcein at 500 nm, 3-PF of DAPI at 333 nm).

Two-photon fluorescence was used to image and quantitatively characterize the microstructure and cell–substrate interactions within microporous scaffold substrates fabricated from synthetic biodegradable polymers [130]. The authors seeded GFP-labelled fibroblasts in Texas red-labelled poly-(DTE/DTO) carbonate blend scaffolds of varying porosity and studied the spatial distribution of micro- and macroporous regions and cell morphology patterns (e.g. cytoskeletal organization). Parameters such as porosity, pore size and distribution, strut size, pore interconnectivity and orientation of both macro- and micro-scale pores were quantified and validated. Two-PF enables image acquisition from depths larger than 100 µm with high signal-to-noise ratio and reduced photobleaching. NLOM is a promising integrated platform for imaging of cell–material interactions within the interior of polymeric biomaterials.

As the success of TE depends largely on the rapid and efficient formation of functional blood vessel architectures, some authors used 2-PF to image and analyse scaffold vascularization [131]. PLLA scaffolds (Matrigel-enriched with basement membrane proteins) were seeded with human endothelial and red fluorescent protein (RFP)-expressing smooth muscle cells and implanted subcutaneously into immune-deficient mice. *In vivo*, endothelial and vascular smooth muscle cells assembled a patent microvasculature that anastomosed with the host circulation during the first week of implantation. After two weeks, animals were injected with FITC-labelled lectin to selectively label endothelial cells. Multiphoton fluorescence angiographic analysis of the intra-scaffold microcirculation showed a uniform, branched micro-vascular network. Three-dimensional image reconstruction analysis of smooth muscle cell distribution implants was non-random and displayed a preferentially perivascular localization. The results show that 2-PF can be applied for imaging scaffold vascularization in an *in vivo* TE context.

### 3.3. Second harmonic generation microscopy

SHG has many features in common with 2-PF (penetration depth); however, no energy is deposited in the sample (100% energy conversion; figure 3*a*), and no bleaching or heating effects should occur even with high laser powers or in long-term observations [132]. Nevertheless, the required high laser intensities may cause photodamaging effects derived from still-present AF. SHG is a label-free and highly specific technique. Its occurrence is connected to physical features of certain molecules and molecule assemblies. SHG-susceptible molecules lack a centro-symmetry [133,134]. Additionally, they fulfil the phase-matching condition, i.e. the incident and the resulting second harmonic wave travel with the same velocity. This is because nonlinear frequency conversion is only efficient in a coherent situation, when the SHG waves generated by different molecules are in phase and interfere constructively. This condition is only met by materials with a high degree of organization and orientation, such as anisotropic crystals or certain structural protein arrays, i.e. SHG has a very high specificity for these structures [132,135].

#### 3.3.1. Imaging cellular proteins

Only a limited number of biological structures show strong SHG susceptibilities. By far, the most important ones are assembled collagen I fibres [135], myosin II (actomyosin in muscle cells) and tubulin (basic unit of microtubules, which are part of the cytoskeleton). By far, the most important structure used in TE research is represented by collagen [136–138]. The methodology is sensitive to changes that occur in

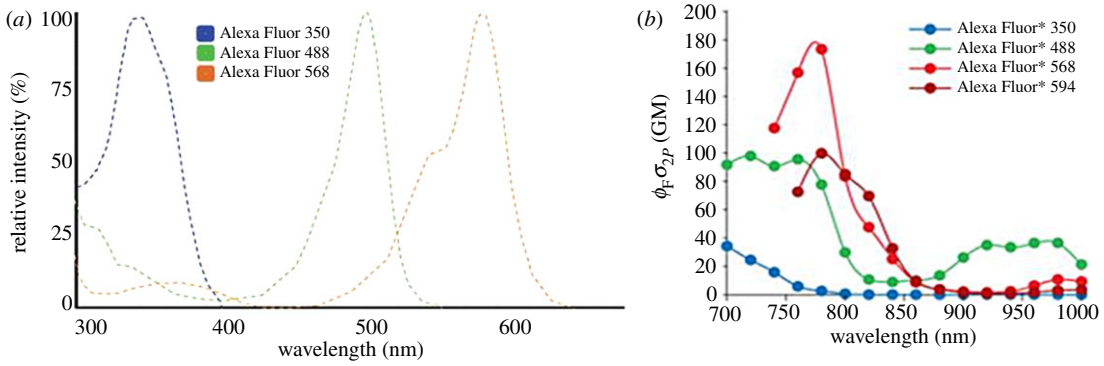


(c)

| dye | labelling | excitation (nm) | | | emission (nm) |
|---|---|---|---|---|---|
| | | 1-PF | 2-PF | 2×1-PF | |
| Alexa 350 | antibody | 350, 450 | 700 | 700, 900 | 440 |
| DAPI, Hoechst | nucleus | 350, 470 | 700*, 740, 780–800, 900–1100 | 700, 940 | 455, 478 |
| DiA | membrane | 455 | 800–860 | 910 | 580 |
| Alexa 488 | antibody | 488 | 720–800, 830 | 976 | 515 |
| FITC | antibody | 490, 525 | 750–800 | 980, 1050 | |
| Calcein AM | cytoplasm | 495 | 900* | 990 | 515 |
| TRITC | antibody | 541, 572 | 800–840 | 1082, 1144 | 572 |
| Cy3 | antibody | 550 | 780 | 1100 | 565, 615 |
| Cy5 | antibody | 649 | 780–820 | 1298 | 670 |

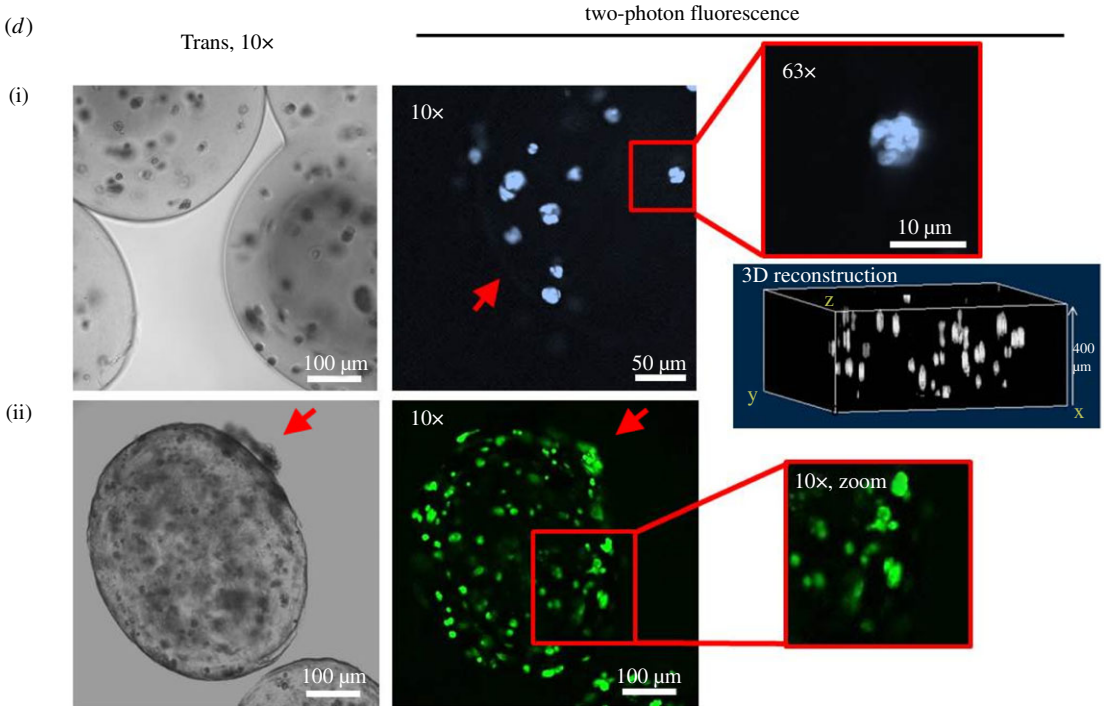


**Figure 6.** Two-photon excitation and imaging of selected fluorescent dyes. (*a*) Normalized one-photon excitation spectra of antibody-conjugated Alexa Fluor 350, 488 and 568 dyes are shown (unconjugated dyes almost identical). Spectra are narrow and well separated. Data from Spectra Viewer software (Invitrogen). (*b*) Two-photon excitation spectra of Alexa Fluor 350, 488, 568 and 594 dyes. The *y*-axis unit Goeppert–Mayer (product of fluorescence quantum yield $\Phi_F$ and two-photon absorption cross section $\sigma$) is a measure of excitation efficiency. These spectra are shaped differently (less well defined and much broader) compared with (A, e.g. Alexa Fluor 488) and maxima are blue-shifted [100,108]. (*c*) Excitation and emission of prominent dyes using one- and two-photon excitation. The table lists a number of commonly used fluorophores (sorted by increasing excitation wavelength). Two-photon excitation maxima are shifted markedly to shorter wavelengths compared with double the wavelengths of one-photon excitation. Emission spectra, however, are identical. Sources: Zeiss publication 'suitable dyes for multiphoton', Xu *et al.* [121], 1-PF values from Spectra Viewer (Invitrogen). Asterisk denotes own observations. Alternatives to Cy and Alexa Fluor dye series with optimized photophysical behaviour are Atto, Chromeo and DyLight dyes. (*d*) Fluorescence-labelled encapsulated MG-63 cells imaged with 2-PF. (i) Cells in alginate-RGD capsules cultured for four weeks were DAPI-stained for nuclei and imaged at 700 nm. The red arrow points to the capsule border (10× image). Nuclear staining even resolved subnuclear segmentation (63×). A three-dimensional reconstruction image generated from image stacks allows quantitative analyses of cell number and distribution. (ii) Calcein-stained cells in alginate cross-linked with gelatin (50 : 50) after six weeks (900 nm). Capsules show a rough and porous surface and are partially non-transparent. Cells migrate through the border to the outer surface of the capsule (red arrows). The cellular calcein distribution allows determination of cell morphology (zoom image). 2-PF allows imaging deep within widely non-transparent capsules.

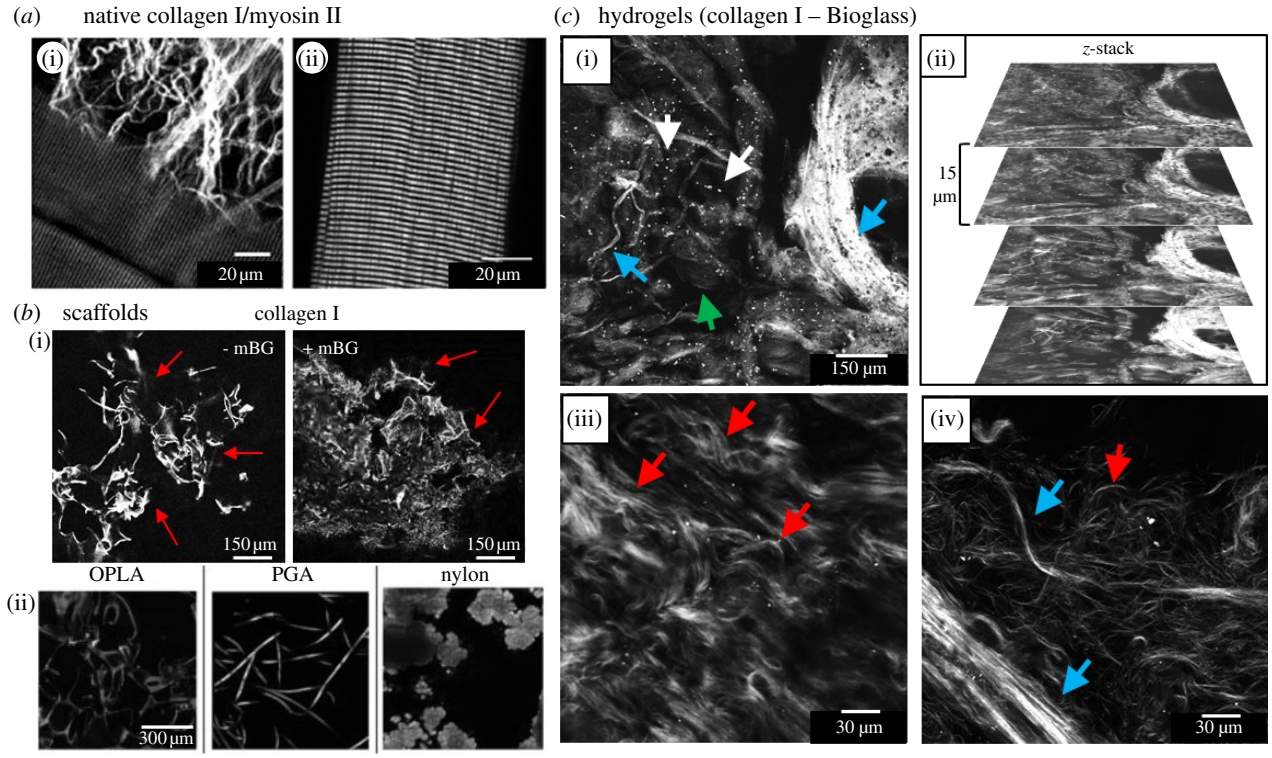


**Figure 7.** SHG imaging of native tissue and various biomaterials. (*a*) SHG signals from muscle fibres and surrounding collagen in an entire murine extensor digitorum longus muscle. Collagen I with its characteristic fibrous form is imaged in (I, red arrow). The muscle-derived signals originate from the regularly ordered myosin filaments visible in (i, blue arrow) and more pronounced in (ii) [147]. (*b*) SHG images of collagen I hydrogels with or without micrometre-sized Bioglass (mBG, mean particle size, 5 µm) after freeze-drying (i, 800 nm, 20× images). Strong SHG signals from collagen (red arrows) allow the determination of scaffold structure and mBG does not significantly alter this structure. (ii) SHG imaging of various TE scaffolding materials. Open-cell poly-lactic acid (OPLA), poly-glycolic acid (PGA) and nylon are shown [36]. (*c*) SHG imaging of hydrogels from composites of collagen I and micrometre-sized Bioglass (800 nm). (i) Collagen fibres (blue arrows) as well as mBG are clearly visible (white arrows). Collagen arranges both in thin fibres and thick fibre bundles. In some less bright regions where no fibres appear (green arrow), the collagen may not be polymerized completely. (ii) Image stack from (i) giving an impression of the three-dimensional structure of the hydrogel. (iii) Red arrows pointing to the typical wavy fibres formed by collagen I from skin. In (iv), fibre bundles (blue arrows) and single fibres (red arrow) are shown in detail. Magnification: (*a*,*d*), 20×; (*b*,*c*), 63×.

diseases such as sclerodermia or in skin or other epithelial cancer types [139–141]. Other application examples are the investigation of heart valves and cardiac [63] or corneal tissue [142,143]. To image collagen I with SHG, excitation wavelengths from 720 to 960 nm [62] can be used, and for detection, a bandpass filter with centre wavelength at half the excitation wavelength is applied (e.g. a 420/20 filter when excitation occurs at 840 nm).

Figure 8*a* shows an interesting approach for long-term monitoring and quantifying tissue morphogenesis by a combined 2-PF/SHG approach [109]. Scaffold and cells were imaged by two-photon AF and collagen I with SHG (both excited at 760 nm). The authors grew human MSCs on chitosan scaffolds and, after TGF-$\beta_3$ stimulation, followed the process of chondrogenesis via the timeline of collagen I production (SHG). After one week, initial fibre production became visible, and after two weeks, fibre distribution and arrangement could be imaged in detail. Bundles of collagen I fibres produced by the cells inside chitosan domains extended into adjacent domains, and massive collagen production was detected after seven weeks. The authors showed that overall collagen production in the scaffold periphery was much stronger than in deeper regions (up to 30 µm), which was explained with limited cell seeding in deeper scaffold regions. Quantitative determination of SHG further demonstrated that the saturation point of collagen production was reached between days 11 and 14. The results showed that qualitative and quantitative multiphoton analysis is an effective technique for non-invasive microscopic examination and monitoring of the quality of engineered tissues. Both scaffold–tissue interaction and the status of synthesized collagen matrix could be imaged without labelling or the use of histological procedures.

SHG imaging of myosin II has been applied to study heart or skeletal muscle tissue [123,144], and imaging of microtubules has been used for the visualization of cell proliferation (interphase and mitotic cells), cancer cells and the axons of neurons [145,146]. In figure 7*a*, SHG images highlight myosin II and collagen I structures in isolated mouse muscle fibres. In image (i), extracellular collagen I fibres surrounding the muscle cells can be seen and in image (ii), the highly ordered structure of the actomyosin becomes visible, in which the SHG effect originates from the biocrystalline structure of the anisotropic bands (A bands) of the sarcomeres (myosin rods).

### 3.3.2. Biomaterial imaging

For TE purposes, collagen I is often used as a scaffolding material to provide seeded cells with an artificial ECM. By using self-assembled hydrogels, collagen I networks and their properties can be studied in detail with and without cells. Here, interesting parameters are collagen assembly, fibre length and thickness, pore size distribution and mechanical and rheological properties of the hydrogels [82,137,148]. Some authors have studied the aspect of cell

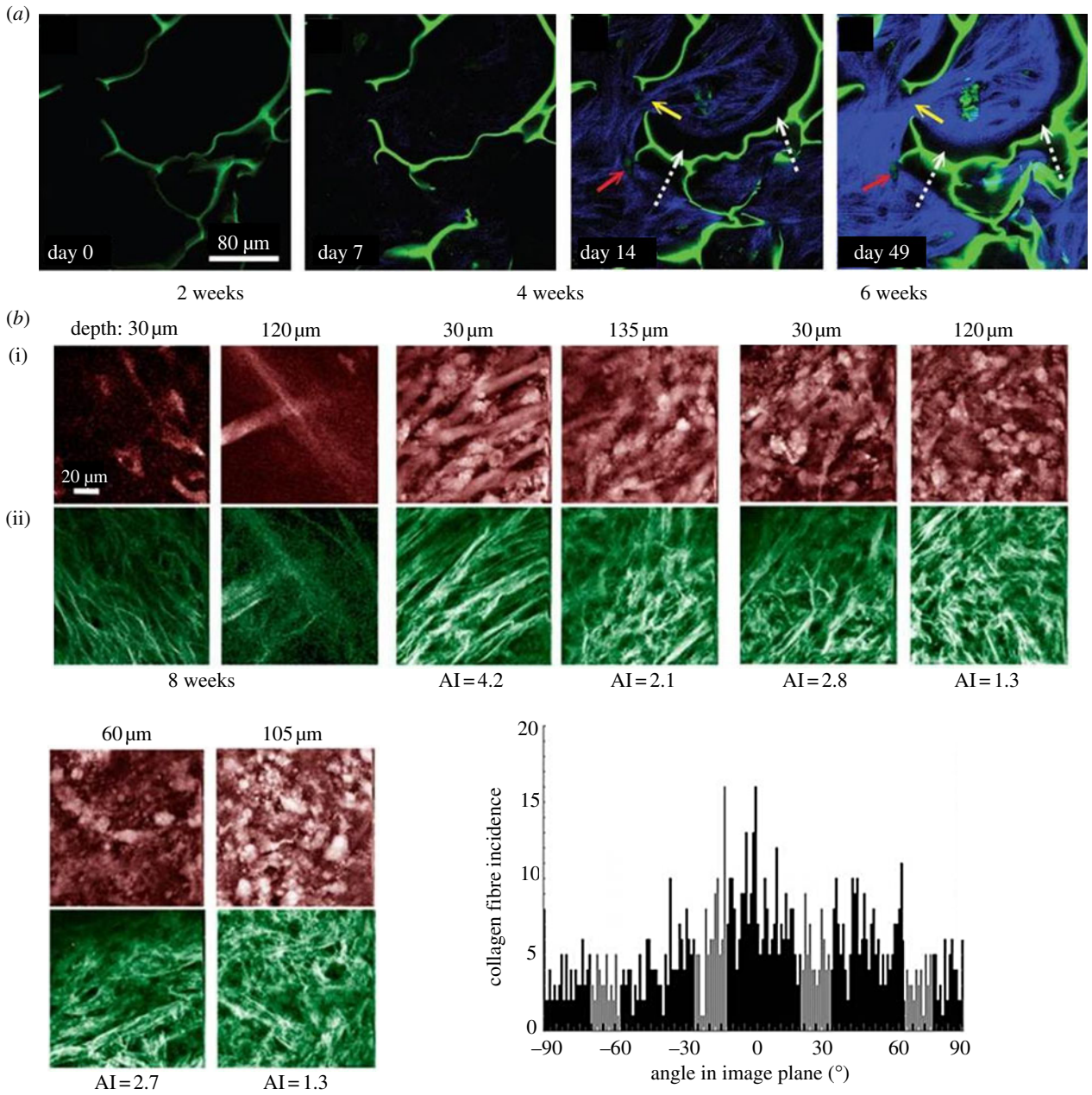


**Figure 8.** Timeline and SHG imaging of collagen I production. (*a*) Multiphoton images from human MSCs cultured in a chitosan scaffold that were induced to undergo chondrogenesis (TGF-β3) for up to seven weeks [109]. Images were acquired at a depth of 15 µm. Two-photon AF is represented in green (scaffold boundaries and cells) and SHG in blue (produced collagen I). The cells massively produce ECM after two weeks. The lack of contact between the induced collagen fibres and the chitosan scaffold is shown by the white dashed arrows, and the linkages formed by the collagen from adjacent chitosan domains are shown by the yellow arrows. The red arrows show the lacunae-like structures that have been formed within collagen clusters, with autofluorescent cells inside. (*b*) Collagen fibre orientation analysis. NLOM images of constructs from two to eight weeks of culture. Pseudo-coloured images of PGA polymer and smooth muscle cells (AF, red (i)) and collagen fibres (SHG, green (ii)). Fibres of PGA scaffold were clearly visible at two and four weeks, with collagen deposition running parallel to PGA fibres. From four to eight weeks, local collagen alignment with PGA fibres decreased as the PGA degraded, as revealed by an alignment index (AI) computed for the collagen fibres at weeks four to eight. Depth of image acquisition is shown in micrometres. The scale bar (20 µm) applies to all images. The histogram (bottom left) shows a projection of all collagen fibre angles from the eight week specimen [136].

behaviour in collagen I hydrogels. For example, Lee *et al.* [149] have revealed that invading endothelial cells anisotropically alter three-dimensional collagen matrices by a combined approach of SHG and 2-PF imaging. Yannas *et al.* [150] review the processing and characterization of collagen-based scaffolds in detail.

In SHG imaging experiments, we have used collagen I—micrometre-sized Bioglass 45S5 composite hydrogels that represent a promising biomaterial combination in bone TE [15]. In figure 7*c*(i–iv), both collagen I and Bioglass were resolved with micrometre resolution. Collagen I was present either as thin fibres and fibre bundles of varying thickness (i,iv). Images (iii) and (iv) give an impression of the collagen network and the typically wavy fibre form known from collagen in skin (iii). By stacking multiple images (ii), typical fibre lengths could be determined (by three-dimensional reconstruction). Fibre length is an important parameter of hydrogel rheological properties and for optimizing cell growth in hydrogels. We have also produced and imaged freeze-dried scaffolds (sponges, foams) from collagen I with and without micrometre-sized Bioglass, which can be cross-linked and seeded with target cells [151–153]. We obtained

SHG images from these scaffolds (figure 7*b*(i)) and by using three-dimensional stacks and reconstructions, it was possible to characterize the scaffolds porous structure (not shown). Similar findings were obtained by Sun *et al.* [36], who imaged comparable scaffolds (collagen I and Collagraft bone matrix strip) and additional TE-relevant scaffolding materials (e.g. PGA, open-cell PLA, nylon; figure 7*b*(ii)) with SHG. The authors state that the nonlinear optical properties of the scaffolds will enable us to spectrally and morphologically distinguish the different types of scaffold materials investigated. The SHG results demonstrate that a number of artificial organic polymers are susceptible to SHG. Further, very interesting and promising SHG-susceptible biomaterials that are frequently being used in TE research are cellulose [12,76,141,154], silk [119], gelatin/collagen gels [13,137] or PHB/PHBHHx [155]. A review by Dempsey *et al.* [132] identifies small particles that are widely used in TE to enhance scaffold mechanical stability or to track cells (e.g. Bioglass, nanodiamonds, Qdots) are susceptible to SHG as well.

## 3.4. Multi-modal and quantitative analysis

A large number of studies have used multiple imaging modalities (2-PF, SHG, CARS) to simultaneously image cells, ECM and scaffold. Cell arrangement on and within the scaffolds, cell–scaffold interactions as well as production and arrangement of ECM proteins, cell differentiation and tissue morphogenesis are of common interest in most studies, and a large number of different biomaterials and cells (primary cells, cell lines and stem cells) from bone, cartilage, cardiovascular, connective and adipose tissue were used for this purpose. A large number of studies used NLOM for quantitative analysis of ECM fibre distribution, effects of biomechanical treatment or cell metabolic state. This underlines that NLOM techniques are very powerful and flexible tools beyond simple structure visualization.

In a study by Brackmann *et al.* [76] simultaneous SHG/CARS imaging was applied for visualizing osteoprogenitor cell three-dimensional arrangement in a microporous cellulose scaffold (cells and scaffold: CARS). Unexpectedly, cells produce collagen I (marker for osteogenesis, SHG) already during the first days of growth, which demonstrates that cellulose is a potential scaffold material for bone TE. The authors state that the combined *in situ* monitoring with CARS/SHG is suitable for TE studies. In a comparable study by Filova *et al.* [13], a 2-PF/SHG approach was chosen for analysing production and spatial arrangement of collagen (SHG) by isolated chondrocytes (labelled with Cy3-coupled antibody, 2-PF) and spatial cell arrangement (nuclear staining, 2-PF) in a gelatin–PCL scaffold at 860 nm excitation wavelength. This novel approach represents a powerful tool for the analysis of collagen-containing scaffolds with applications in cartilage TE. Mouras *et al.* [73] have followed the process of MSC differentiation with a combination of two-photon AF (cells), SHG (collagen I) and CARS imaging (lipids at 1064 nm, HA crystals at 867 nm). The authors report that they were able to monitor and quantify the differentiation into osteoblasts (verified by collagen I and HA formation) and adipocytes (lipid production).

Taking advantage of differential two-photon AF emission of NADH/NAD and FAD, Quinn *et al.* [68] developed cell metabolic readouts using ratiometric measurements of these metabolic cofactors. The authors state that it was possible to reliably determine the metabolic status of cultured cells by their two-photon AF characteristics. The same principle has been used for online monitoring of tissue maturation. TE largely depends on the control of culture conditions and tissue maturation, and methods for monitoring the effects of stimuli and induced tissue changes are of key interest. For tracking stem cell osteogenic differentiation, Rice *et al.* [74] have used both two-photon AF (NADH, flavoprotein and lipofuscin concentrations) and SHG (collagen I). Redox ratio imaging over time (calculated from the contributions of NADH and flavins) changes in cell morphology (AF) and simultaneous SHG provided information on the status of the osteogenic process. In addition, lipofuscin was found to be a potential biomarker for oxidative stress. The authors' conclusion was that it is possible to monitor engineered tissues and optimize culture conditions in a near real-time manner.

Another field for analysis is found in the quantitation of ECM fibre production and orientation analysis, for example, in biomechanical studies. In order to improve collagen architecture and mechanical properties, engineered tissues have to be mechanically stimulated. In a study by Rubbens *et al.* [125], the influence of biomechanical stimulation on growing myofibroblasts has been analysed using dual-colour CellTracker blue and fluorescently labelled collagen I markers (2-PF). The authors quantified collagen fibre organization in response to varied mechanical stimulation (normal culture versus an intermittent stretching condition) mimicking the native biomechanical behaviour, which is a major goal in cardiovascular TE. Mechanical loading induced collagen alignment, which was improved by applying intermittent strain. Comparable studies have been carried out by Hu *et al.* [156], who characterized tissue development under biaxial stretch using fibroblast-seeded or cell-free collagen gels. The collagen I fibre orientations (SHG) revealed contributions of applied stretches, of cell-mediated tractions and matrix remodelling on the measured fibre distributions. The authors concluded that the integration of intravital NLOM with novel bioreactors enables imaging of dynamic tissue properties in culture. Niklason *et al.* [136] developed mathematical models of growth and remodelling of engineered tissues cultured on polymeric scaffolds and applied NLOM for their verification (figure 8*b*). Collagen fibre distributions were quantitatively analysed in two depths within the tissue over eight weeks of culture. A cumulative plot of fibre orientations (histogram) revealed four predominant collagen fibre families that were centred approximately at $0^\circ$, $\pm 45^\circ$ and $90^\circ$ and are consistent with prior TEM imaging observations and model predictions.

## 3.5. Three-photon-based nonlinear optical microscopy techniques

In three-photon excitation, three photons provide one-third each of the energy required to reach the excited state. Wavelengths beyond 1200 nm must be used, which requires an OPO. The longer wavelengths penetrate tissues even deeper and are less damaging. However, the higher order of nonlinearity means even weaker signals [157]. Because this consequently requires higher photon fluxes, three-photon-based technique has not been used as extensively as the two-photon-based ones. Relevant techniques for tissue imaging are CARS, THG and 3-PF microscopy.

**Table 2.** NLOM methods: pros and cons. The techniques are widely complementary and may be combined in multi-modal NLOM applications.

| | 2-PF/3-PF | SHG/THG | CARS |
|---|---|---|---|
| + | autofluorescent molecules can be used for imaging | high-contrast method without staining | chemically selective, imaging of cell and organelle boundaries (membranes) |
| | very large number of fluorophores may be imaged including Qdots (almost like 1-PF) | completely non-invasive technique | completely non-invasive technique |
| | excitation spectra broader than in 1-PF: more flexibility, easier multicolour applications | no photobleaching, no energy left behind in tissue | no photobleaching (long-term investigations) |
| | by using antibodies in principle all molecules may be visualized | large excitation range possible (flexibility) | excellent imaging of lipid distribution and osteodifferentiation (hydroxylapatite formation) |
| | 3-PF: additional spectrum of molecules excitable in the UV accessible; higher tissue penetration (longer excitation wavelengths) | SHG: biomaterials can be imaged<br>THG: imaging of interfaces possible, higher tissue penetration (longer wavelengths) | applicable inside the body (endoscopy) |
| − | photobleaching and thermal damage | SHG: limited to a low number of molecules | expensive and high complexity technique |
| | stainings are often required | SHG: to image collagen I, the molecule needs to be highly assembled | limited to small number of observable molecules |

CARS imaging derives its optical contrast directly from Raman-active vibrational characteristics of certain molecules (label-free) and is capable of chemically selective, highly sensitive and high-speed imaging without photobleaching. CARS microscopy uses two laser beams, a pump beam at frequency $\omega_p$ and a Stokes beam at frequency $\omega_S$. When the beat frequency ($\omega_p - \omega_S$) matches the frequency of a particular Raman-active molecular vibration ($\omega_{vib}$), the resonant oscillators are coherently driven, resulting in a strong anti-Stokes signal at $\omega_{as} = 2\omega_p - \omega_S$ [158]. The technique was applied to study osteogenic and adipogenic differentiation [73], scaffolds and hydrogels [12,76,159,160], vascular and neurodegenerative diseases [38,161] and drug delivery and subcellular distribution (reviewed in Strachan *et al.* [162]). CARS microscopy has proved useful for mapping lipid compartments in various tissues and cells [158,163], protein clusters [164] and water distributions [161] in cell tissue cultures and has been used with great success for imaging of many types of lipids (C–H vibration) and phosphates [165]. State-of-the-art CARS microscopes have high enough sensitivity to detect single lipid bilayers [163].

THG imaging is another relevant technology. One advantage of THG over SHG is that the requirement for non-inversion symmetry of the molecules to be excited is revoked [27]. This makes THG sensitive for interfaces and heterogeneities and for the detection of membranes and membrane-based organelles, blood vessels and other biological structures [31,162,166]. Another application is imaging of lipid bodies which are ubiquitous structures present in many cells and tissues with many different functions. Disorders of lipid regulation occur in common diseases such as atherosclerosis, diabetes and steatosis. As lipid bodies are generally non-fluorescent, their direct imaging with THG offers interesting perspectives. Debarre *et al.* [167] have used THG to quantify lipid metabolism in isolated hepatocytes, but this approach is relevant to adipocytes and also liver and intestine cells. THG can further be used to study drug release systems (visualize uptake mechanisms of pharmaceuticals) and distribution of nanosized particles (e.g. in skin) and many other applications [162]. The main benefit of 3-PF is the excitation of molecules that absorb in the UV (e.g. the amino acid tryptophane at 266 nm), which allows label-free imaging of intrinsic protein fluorescence [168]. Other authors have used 3-PF for label-free imaging of neurotransmitters such as serotonin and dopamine, which has implications for neuronal TE [157,169].

## 3.6. Nonlinear optical microscopy techniques: advantages and disadvantages

NLOM techniques have multiple advantages over one-photon excitation-based CFM. These include the issues of photobleaching, phototoxicity, significantly enhanced imaging depth in opaque scaffolds, staining requirement and signal intensity. However, none of the discussed NLOM techniques is perfect, and all methods have their specific strengths and limitations when compared with each other. Table 2 gives an overview of all the benefits and problems encountered with the different multiphoton techniques explained in this review. Summarized shortly, 2-PF always produces a certain amount of photobleaching or requires additional staining, but on the other side, in principle, any kind of molecule can be addressed and thus, visualized by using antibody labelling. SHG and CARS, on the other hand, are basically non-invasive, but altogether quite specialized techniques and therefore, limited to a rather low number of possible applications. The techniques also require

sophisticated and extensive optical equipment and are thus, not readily available.

## 4. Summary and outlook

The classical methods for visualizing tissues, biomaterials and scaffolds such as μCT/MRI/OCT and histology in combination with optical and electron microscopy have a number of limitations concerning invasiveness and artefact production, resolution, tissue penetration and requirement for labelling. Quite often, only the combined use of complementary methods leads to strong and clear results. NLOM overcomes many of these problems and enables deep-tissue imaging with high resolution without destructive labelling procedures, because intrinsic sources of contrast are used. NLOM methods are further suitable to track and thereby to control the development of engineered tissues online in long-term experiments. NLOM imaging in TE encompasses a number of techniques for the study of scaffolds (surface and inner structure), cells (distribution, morphology, metabolic state, vascularization) and ECM. Multiphoton fluorescence is used to visualize cells by their natural autofluorescence and to image (immune-)labelled structures. Label-free and highly specific imaging techniques are SHG and CARS. SHG is commonly used to image ECM (collagen I), cytoskeleton (microtubules), myosin II (actomyosin) in muscle cells and a number of biomaterials, whereas CARS is the method of choice for visualizing membranes and lipid distributions within cells and tissues. Combinations of NLOM methods have been successfully applied to study cell differentiation (osteogenesis, adipogenesis) and tissue maturation (by abundance and arrangement of collagen I fibres). Quantification of collagen fibre orientation has been used as a powerful tool to study the response of engineered tissues to mechanical loading.

Recent advances in detection schemes (faster and higher-sensitivity detectors, multifocal imaging), more powerful laser sources, better optical components, a deeper understanding of contrast mechanisms and more sophisticated analysis tools will further increase the performance of NLOM imaging. Especially, THG and CARS, but also spectroscopic techniques such as fluorescence correlation spectroscopy (FCS) or fluorescence lifetime imaging microscopy (FLIM) will become more important. Progress in the field of biomaterials and processing techniques (e.g. tissue and organ printing) will deliver better scaffolds of higher and more directed functionality (drug delivery, controlled growth factor release, degradation and vascularization, cell attraction *in vivo* that will more closely resemble native tissue). NLOM imaging will promote TE with its high degree of experimental flexibility. It can be used for intravital imaging of tissue development in bioreactors, *in vivo* (multiphoton endoscopy) and with tissue models (e.g. skin, liver) and models of cancer or atherosclerosis. This way, NLOM will improve the study of healthy as well as malfunctioning tissue. Emerging applications, such as metabolite and drug imaging or tumour identification, raise many exciting new possibilities for medicine and biology.

Acknowledgements. The authors thank A. Grigore, B. Sarker, A. Grünewald, J. Hum and T. Zehnder for providing various materials and U. Wenig and R. Stadler for enabling experiments with the MP5 microscope. O.F. acknowledges ongoing support from the Erlangen Graduate School of Advanced Optical Technologies (SAOT) within the German Excellence Cluster funding scheme.

Funding statement. This work was supported by the Emerging Fields Initiative (EFI) project TOPbiomat from the Friedrich-Alexander University of Erlangen-Nuremberg.

## References

1. Watt SM, Athanassopoulos A, Harris AL, Tsaknakis G. 2010 Human endothelial stem/progenitor cells, angiogenic factors and vascular repair. *J. R. Soc. Interface* **7**, S731–S751. (doi:10.1098/rsif.2010.0377.focus)
2. Place ES, Evans ND, Stevens MM. 2009 Complexity in biomaterials for tissue engineering. *Nat. Mater.* **8**, 457–470. (doi:10.1038/nmat2441)
3. Langer R, Vacanti JP. 1993 Tissue engineering. *Science* **260**, 920–926. (doi:10.1126/science.8493529)
4. Turner NJ, Ph D, Yates AJ, Weber DJ, Qureshi IR, Stolz DB, Gilbert TW, Badylak SE. 2010 Xenogeneic extracellular matrix as an inductive scaffold for regeneration of a functioning musculotendinous junction. *Tissue Eng.* **16**, 3309–3317. (doi:10.1089/ten.tea.2010.0169)
5. Lee J, Cuddihy MJ, Kotov NA. 2008 Three-dimensional cell culture matrices: state of the art. *Tissue Eng. B, Rev.* **14**, 61–86. (doi:10.1089/teb.2007.0150)
6. Rai MF, Graeve T, Twardziok S, Schmidt MFG. 2011 Evidence for regulated interleukin-4 expression in chondrocyte-scaffolds under *in vitro* inflammatory conditions. *PLoS ONE* **6**, e25749. (doi:10.1371/journal.pone.0025749)
7. Yang X, Zhang S, Pang X, Fan M. 2012 Pro-inflammatory cytokines induce odontogenic differentiation of dental pulp-derived stem cells. *J. Cell Biochem.* **113**, 669–677. (doi:10.1002/jcb.23396)
8. Liang M-S, Andreadis ST. 2011 Engineering fibrin-binding TGF-β1 for sustained signaling and contractile function of MSC based vascular constructs. *Biomaterials* **32**, 8684–8693. (doi:10.1016/j.biomaterials.2011.07.079)
9. McBane JE, Cai K, Labow RS, Santerre JP. 2012 Co-culturing monocytes with smooth muscle cells improves cell distribution within a degradable polyurethane scaffold and reduces inflammatory cytokines. *Acta Biomater.* **8**, 488–501. (doi:10.1016/j.actbio.2011.09.018)
10. Pandit A, Ashar R, Feldman D. 1999 The effect of TGF-beta delivered through a collagen scaffold on wound healing. *J. Invest. Surg.* **12**, 89–100. (doi:10.1080/089419399272647)
11. Chim H, Miller E, Gliniak C, Alsberg E. 2012 Stromal-cell-derived factor (SDF) 1-alpha in combination with BMP-2 and TGF-β1 induces site-directed cell homing and osteogenic and chondrogenic differentiation for tissue engineering without the requirement for cell seeding. *Cell Tissue Res.* **350**, 89–94. (doi:10.1007/s00441-012-1449-x)
12. Brackmann C, Dahlberg J, Vrana NE, Lally C, Gatenholm P, Enejder A. 2012 Non-linear microscopy of smooth muscle cells in artificial extracellular matrices made of cellulose. *J. Biophotonics* **5**, 404–414. (doi:10.1002/jbio.201100141)
13. Filova E, Burdikova Z, Rampichova M, Bianchini P, Capek M, Kostakova E, Amler E, Kubinova L. 2010 Analysis and three-dimensional visualization of collagen in artificial scaffolds using nonlinear microscopy techniques. *J. Biomed. Opt.* **15**, 066011. (doi:10.1117/1.3509112)
14. Pancrazio JJ, Wang F, Kelley CA. 2007 Enabling tools for tissue engineering. *Biosens. Bioelectron.* **22**, 2803–2811. (doi:10.1016/j.bios.2006.12.023)
15. Marelli B, Ghezzi CE, Barralet JE, Boccaccini AR, Nazhat SN. 2010 Three-dimensional mineralization of dense nanofibrillar collagen–bioglass hybrid

scaffolds. *Biomacromolecules* **11**, 1470–1479. (doi:10.1021/bm1001087)

16. Georgakoudi I, Rice WL, Hronik-Tupaj M, Kaplan DL. 2008 Optical spectroscopy and imaging for the noninvasive evaluation of engineered tissues. *Tissue Eng. B, Rev.* **14**, 321–340. (doi:10.1089/ten.teb.2008.0248)
17. Xu H, Othman SF, Magin RL. 2008 Monitoring tissue engineering using magnetic resonance imaging. *J. Biosci. Bioeng.* **106**, 515–527. (doi:10.1263/jbb.106.515)
18. Jones JR, Atwood RC, Poologasundarampillai G, Yue S, Lee PD. 2009 Quantifying the 3D macrostructure of tissue scaffolds. *J. Mater. Sci. Mater. Med.* **20**, 463–471. (doi:10.1007/s10856-008-3597-9)
19. Young S, Kretlow JD, Nguyen C, Bashoura AG, Baggett LS, Jansen JA, Wong M, Mikos AG. 2008 Microcomputed tomography characterization of neovascularization in bone tissue engineering applications. *Tissue Eng.* **14**, 295–306. (doi:10.1089/ten.teb.2008.0153)
20. Ballyns JJ, Bonassar LJ. 2010 Image-guided tissue engineering. *J. Cell. Mol. Med.* **13**, 1428–1436. (doi:10.1111/j.1582-4934.2009.00836.x)
21. Vande Velde G, Baekelandt V, Dresselaers T, Himmelreich U. 2009 Magnetic resonance imaging and spectroscopy methods for molecular imaging. *Q. J. Nucl. Med. Mol. Imaging* **53**, 565–585.
22. Zheng K, Rupnick MA, Liu B, Brezinski ME. 2009 Three dimensional OCT in the engineering of tissue constructs: a potentially powerful tool for assessing optimal scaffold structure. *Open Tissue Eng. Regen. Med.* **2**, 8–13. (doi:10.2174/1875043500902010008)
23. Liang X, Graf BW, Boppart SA. 2009 Imaging engineered tissues using structural and functional optical coherence tomography. *J. Biophotonics* **2**, 643–655. (doi:10.1002/jbio.200910048)
24. Boppart S, Oldenburg A, Xu C, Marks D. 2005 Optical probes and techniques for molecular contrast enhancement in coherence imaging. *J. Biomed. Opt.* **10**, 41208. (doi:10.1117/1.2008974)
25. Smith LE, Smallwood R, Macneil S. 2010 A comparison of imaging methodologies for 3D tissue engineering. *Microsc. Res. Tech.* **73**, 1123–1133. (doi:10.1002/jemt.20859)
26. Muller M. 2006 *Introduction to confocal fluorescence microscopy*, 2nd edn. Bellingham, WA: SPIE Press.
27. Ustione A, Piston DW. 2011 A simple introduction to multiphoton microscopy. *J. Microsc.* **243**, 221–226. (doi:10.1111/j.1365-2818.2011.03532.x)
28. Doroski DM, Brink KS, Temenoff JS. 2007 Techniques for biological characterization of tissue-engineered tendon and ligament. *Biomaterials* **28**, 187–202. (doi:10.1016/j.biomaterials.2006.08.040)
29. Dawes C. 1979 *Biological techniques for transmission and scanning electron microscopy*. Burlington, VT: Ladd Research Industries, Inc.
30. Grandfield K, Palmquist A, Engqvist H. 2012 High-resolution three-dimensional probes of biomaterials and their interfaces. *Phil. Trans. R. Soc. A* **370**, 1337–1351. (doi:10.1098/rsta.2011.0253)
31. Carriles R, Schafer DN, Sheetz KE, Field JJ, Cisek R, Barzda V, Sylvester AW, Squier JA. 2009 Invited review article: imaging techniques for harmonic and multiphoton absorption fluorescence microscopy. *Rev. Sci. Instrum.* **80**, 081101. (doi:10.1063/1.3184828)
32. Diaspro A, Bianchini P, Vicidomini G, Faretta M, Ramoino P, Usai C. 2006 Multi-photon excitation microscopy. *Biomed. Eng. Online* **5**, 36. (doi:10.1186/1475-925X-5-36)
33. Diaspro A, Chirico G, Collini M. 2005 Two-photon fluorescence excitation and related techniques in biological microscopy. *Q. Rev. Biophys.* **38**, 97–166. (doi:10.1017/S0033583505004129)
34. Schenke-Layland K, Riemann I, Damour O, Stock UA, König K. 2006 Two-photon microscopes and *in vivo* multiphoton tomographs: powerful diagnostic tools for tissue engineering and drug delivery. *Adv. Drug Delivery Rev.* **58**, 878–896. (doi:10.1016/j.addr.2006.07.004)
35. Yeh AT, Gibbs H, Hu J-J, Larson AM. 2008 Advances in nonlinear optical microscopy for visualizing dynamic tissue properties in culture. *Tissue Eng.* **14**, 119–131. (doi:10.1089/teb.2007.0284)
36. Sun YEN *et al*. 2008 Imaging tissue engineering scaffolds using multiphoton microscopy. *Microsc. Res. Tech.* **71**, 140–145. (doi:10.1002/jemt.20537)
37. Niesner RA, Hauser AE. 2011 Recent advances in dynamic intravital multi-photon microscopy. *Cytometry A, J. Int. Soc. Anal. Cytol.* **79**, 789–798. (doi:10.1002/cyto.a.21140)
38. Le TT, Yue S, Cheng J-X. 2010 Shedding new light on lipid biology with coherent anti-Stokes Raman scattering microscopy. *J. Lipid Res.* **51**, 3091–3102. (doi:10.1194/jlr.R008730)
39. Boos AM *et al*. 2012 Engineering axially vascularized bone in the sheep arteriovenous-loop model. *J. Tissue Eng. Regen. Med*. (doi:10.1002/term.1457)
40. Gerhardt L-C *et al*. 2011 The pro-angiogenic properties of multi-functional bioactive glass composite scaffolds. *Biomaterials* **32**, 4096–4108. (doi:10.1016/j.biomaterials.2011.02.032)
41. Saidha S, Eckstein C, Ratchford J. 2010 Optical coherence tomography for the detection of axonal damage in multiple sclerosis. *Ophthalmology* **20**, 77–88. (doi:10.1155/2011/472790)
42. Tan W, Oldenburg AL, Norman JJ, Desai TA, Boppart SA. 2006 Optical coherence tomography of cell dynamics in three-dimensional tissue models. *Opt. Express.* **14**, 7159–7171. (doi:10.1364/OE.14.007159)
43. Smith LE, Bonesi M, Smallwood R, Matcher SJ, Macneil S. 2010 Using swept-source optical coherence tomography to monitor the formation of neo-epidermis in tissue-engineered skin. *J. Tissue Eng. Regen. Med.* **4**, 652–658. (doi:10.1002/term.281)
44. Marelli B, Ghezzi CE, Mohn D, Stark WJ, Barralet JE, Boccaccini AR, Nazhat SN. 2011 Accelerated mineralization of dense collagen-nano bioactive glass hybrid gels increases scaffold stiffness and regulates osteoblastic function. *Biomaterials* **32**, 8915–8926. (doi:10.1016/j.biomaterials.2011.08.016)
45. Baino F, Vitale-Brovarone C. 2011 Three-dimensional glass-derived scaffolds for bone tissue engineering: current trends and forecasts for the future. *J. Biomed. Mater. Res.* **97**, 514–535. (doi:10.1002/jbm.a.33072)
46. Shiels S, Oh S, Bae C, Guda T, Singleton B, Dean DD, Wenke JC, Appleford MR, Ong JL. 2012 Evaluation of BMP-2 tethered polyelectrolyte coatings on hydroxyapatite scaffolds *in vivo*. *J. Biomed. Mater. Res. B* **100**, 1782–1791. (doi:10.1002/jbm.b.32745)
47. Hockaday LA *et al*. 2012 Rapid 3D printing of anatomically accurate and mechanically heterogeneous aortic valve hydrogel scaffolds. *Biofabrication* **4**, 035005. (doi:10.1088/1758-5082/4/3/035005)
48. Sanyal A, Gupta A, Bayraktar HH, Kwon RY, Keaveny TM. 2012 Shear strength behavior of human trabecular bone. *J. Biomech.* **45**, 2513–2519. (doi:10.1016/j.jbiomech.2012.07.023)
49. Woiciechowsky C, Abbushi A, Zenclussen ML, Casalis P, Krüger JP, Freymann U, Endres M, Kaps C. 2012 Regeneration of nucleus pulposus tissue in an ovine intervertebral disc degeneration model by cell-free resorbable polymer scaffolds. *J. Tissue Eng. Regen. Med.* (doi:10.1002/term.1582)
50. Xu J, Chen Y, Yue Y, Sun J, Cui L. 2012 Reconstruction of epidural fat with engineered adipose tissue from adipose derived stem cells and PLGA in the rabbit dorsal laminectomy model. *Biomaterials* **33**, 6965–6973. (doi:10.1016/j.biomaterials.2012.06.010)
51. Luderer F, Begerow I, Schmidt W, Martin H, Grabow N, Bünger CM, Schareck W, Schmitz KP, Sternberg K. 2012 Enhanced visualization of biodegradable polymeric vascular scaffolds by incorporation of gold, silver and magnetite nanoparticles. *J. Biomater. Appl.* (doi:10.1177/0885328212443393)
52. Fercher AF, Drexler W, Hitzenberger CK, Lasser T. 2003 Optical coherence tomography: principles and applications. *Rep. Prog. Phys.* **66**, 239–303. (doi:10.1088/0034-4885/66/2/204)
53. Brezinski ME. 2006 Optical coherence tomography for identifying unstable coronary plaque. *Int. J. Cardiol.* **107**, 154–165. (doi:10.1016/j.ijcard.2005.07.066)
54. Huang D *et al*. 1991 Optical coherence tomography. *Science* **254**, 1178–1180. (doi:10.1126/science.1957169)
55. Yang Y, Dubois A, Qin X, Li J, El Haj A, Wang RK. 2006 Investigation of optical coherence tomography as an imaging modality in tissue engineering. *Phys. Med. Biol.* **51**, 1649–1659. (doi:10.1088/0031-9155/51/7/001)
56. Yang Y, Bagnaninchi PO, Ahearne M, Wang RK, Liu K-K. 2007 A novel optical coherence tomography-based micro-indentation technique for mechanical characterization of hydrogels. *J. R. Soc. Interface* **4**, 1169–1173. (doi:10.1098/rsif.2007.1044)
57. Ishii K, Ma Z, Ninomiya T, Takegoshi M, Kushibiki T, Yamamoto M, Hinds M, Tabata T, Wang RK,

Awazu K. 2007 Control of guided hard tissue regeneration using phosphorylated gelatin and OCT imaging of calcification. *Prog. Biomed. Opt. Imaging Proc. SPIE* 6439: 64390D.

58. Drexler W, Morgner U, Ghanta RK, Kärtner FX, Schuman JS, Fujimoto JG. 2001 Ultrahigh-resolution ophthalmic optical coherence tomography. *Nat. Med.* **7**, 502–507. (doi:10.1038/86589)
59. Liu B, Brezinski ME. 2007 Theoretical and practical considerations on detection performance of time domain, Fourier domain, and swept source optical coherence tomography. *J. Biomed. Opt.* **12**, 044007. (doi:10.1117/1.2753410)
60. Martínez H, Brackmann C, Enejder A, Gatenholm P. 2012 Mechanical stimulation of fibroblasts in micro-channeled bacterial cellulose scaffolds enhances production of oriented collagen fibers. *J. Biomed. Mater. Res.* **100**, 948–957. (doi:10.1002/jbm.a.34035)
61. Chung I, Enemchukwu N, Khaja SD, Murthy N, García AJ. 2009 Bioadhesive hydrogel microenvironments to modulate epithelial morphogenesis. *Biomaterials* **29**, 2637–2645. (doi:10.1016/j.biomaterials.2008.03.008)
62. Schenke-Layland K. 2008 Non-invasive multiphoton imaging of extracellular matrix structures. *J. Biophotonics* **1**, 451–162. (doi:10.1002/jbio.200810045)
63. Schenke-Layland K *et al*. 2009 The use of three-dimensional nanostructures to instruct cells to produce extracellular matrix for regenerative medicine strategies. *Biomaterials* **30**, 4665–4675. (doi:10.1016/j.biomaterials.2009.05.033)
64. Torkian BA, Yeh AT, Engel R, Sun C-H, Tromberg BJ, Wong BJF. 2004 Modeling aberrant wound healing using tissue-engineered skin constructs and multiphoton microscopy. *Arch. Facial Plast. Surg.* **6**, 180–187. (doi:10.1001/archfaci.6.3.180)
65. Kiernan J. 1999 *Histological & histochemical methods: theory and practice*, 3rd edn. Oxford, UK: Butterworth Heinemann.
66. Kneser U *et al*. 2006 Engineering of vascularized transplantable bone tissues: induction of axial vascularization in an osteoconductive matrix using an arteriovenous loop. *Tissue Eng.* **12**, 1721–1731. (doi:10.1089/ten.2006.12.1721)
67. Kinikoglu B, Auxenfans C, Pierrillas P, Justin V, Breton P, Burillon C, Hasirci V, Damour O. 2009 Reconstruction of a full-thickness collagen-based human oral mucosal equivalent. *Biomaterials* **30**, 6418–6425. (doi:10.1016/j.biomaterials.2009.08.010)
68. Quinn KP, Bellas E, Fourligas N, Lee K, Kaplan DL, Georgakoudi I. 2012 Characterization of metabolic changes associated with the functional development of 3D engineered tissues by non-invasive, dynamic measurement of individual cell redox ratios. *Biomaterials* **33**, 5341–5348. (doi:10.1016/j.biomaterials.2012.04.024)
69. Skardal A, Zhang J, Mccoard L, Xu X, Oottamasathien S, Prestwich GD. 2010 Photocrosslinkable hyaluronan–gelatin hydrogels for two-step bioprinting. *Tissue Eng.* **16**, 1675–1685.
70. Iqbal K, Khan Y, Minhas LA. 2012 Effects of immobilization on thickness of superficial zone of articular cartilage of patella in rats. *Indian J. Orthop.* **46**, 391–394. (doi:10.4103/0019-5413.98826)
71. Roldán JC, Chang E, Kelantan M, Jazayeri L, Deisinger U, Detsch R, Reichert TE, Gurtner GC. 2010 Quantifying migration and polarization of murine mesenchymal stem cells on different bone substitutes by confocal laser scanning microscopy. *J. Cranio-Maxillo-Facial Surg.* **38**, 580–588. (doi:10.1016/j.jcms.2010.01.004)
72. Schenke-Layland K *et al*. 2007 Optimized preservation of extracellular matrix in cardiac tissues: implications for long-term graft durability. *Ann. Thorac. Surg.* **83**, 1641–1650. (doi:10.1016/j.athoracsur.2006.12.005)
73. Mouras R, Bagnaninchi P, Downes A, Muratore M, Elfick A. 2011 Nonlinear optical microscopy of adipose-derived stem cells induced towards osteoblasts and adipocytes. *Proc. SPIE* 8086, Advanced Microscopy Techniques II, 80860Q (8 June 2011). (doi:10.1117/12.889780)
74. Rice WL, Kaplan DL, Georgakoudi I. 2010 Two-photon microscopy for non-invasive, quantitative monitoring of stem cell differentiation. *PLoS ONE* **5**, e10075. (doi:10.1371/journal.pone.0010075)
75. Polini A, Pisignano D, Parodi M, Quarto R, Scaglione S. 2011 Osteoinduction of human mesenchymal stem cells by bioactive composite scaffolds without supplemental osteogenic growth factors. *PLoS ONE* **6**, e26211. (doi:10.1371/journal.pone.0026211)
76. Brackmann C, Ph D, Zaborowska M, Sc M, Sundberg J, Gatenholm P, Enejder A. 2012 *In situ* imaging of collagen synthesis by osteoprogenitor cells in microporous bacterial cellulose scaffolds. *Tissue Eng.* **18**, 227–234. (doi:10.1089/ten.tec.2011.0211)
77. Cristino S *et al*. 2005 Analysis of mesenchymal stem cells grown on a three-dimensional HYAFF 11-based prototype ligament scaffold. *J. Biomed. Mater. Res.* **73**, 275–283. (doi:10.1002/jbm.a.30261)
78. Erol MM, Mouriño V, Newby P, Chatzistavrou X, Roether JA, Hupa L, Boccaccini AR. 2012 Copper-releasing, boron-containing bioactive glass-based scaffolds coated with alginate for bone tissue engineering. *Acta Biomater.* **8**, 792–801. (doi:10.1016/j.actbio.2011.10.013)
79. Meng D, Rath SN, Mordan N, Salih V, Kneser U, Boccaccini AR. 2011 *In vitro* evaluation of 45S5 bioglass-derived glass–ceramic scaffolds coated with carbon nanotubes. *J. Biomed. Mater. Res.* **99**, 435–444. (doi:10.1002/jbm.a.33185)
80. Dalby MJ, Di Silvio L, Harper EJ, Bonfield W. 1999 *In vitro* evaluation of a new polymethylmethacrylate cement reinforced with hydroxyapatite. *J. Mater. Sci.* **10**, 793–796.
81. Nehal K, Gareau D, Rajadhyaksha M. 2008 Skin imaging with reflectance confocal microscopy. *Semin. Cutan. Med. Surg.* **27**, 37–43. (doi:10.1016/j.sder.2008.01.006)
82. Mickel W, Münster S, Jawerth LM, Vader DA, Weitz DA, Sheppard AP, Mecke K, Fabry B, Schroder-Turk GE. 2008 Robust pore size analysis of filamentous networks from three-dimensional confocal microscopy. *Biophys. J.* **95**, 6072–6080. (doi:10.1529/biophysj.108.135939)
83. Fischer RS, Wu Y, Kanchanawong P, Shroff H, Waterman CM. 2011 Microscopy in 3D: a biologist's toolbox. *Trends Cell Biol.* **21**, 682–691. (doi:10.1016/j.tcb.2011.09.008)
84. Oheim M, Beaurepaire E, Chaigneau E, Mertz J, Charpak S. 2001 Two-photon microscopy in brain tissue: parameters influencing the imaging depth. *J. Neurosci. Methods* **111**, 29–37. (doi:10.1016/S0165-0270(01)00438-1)
85. Dewitt DD, Kaszuba SN, Thompson DM, Stegemann JP. 2009 Collagen I–Matrigel scaffolds for enhanced Schwann cell survival and control of three-dimensional cell morphology. *Tissue Eng.* **15**, 2785–2793 (doi:10.1089/ten.TEA.2008.0406)
86. Shao L, Gao Y, Yan F. 2011 Semiconductor quantum dots for biomedicial applications. *Sensors* (*Basel, Switzerland*) **11**, 11 736–11 751. (doi:10.3390/s111211736)
87. Chen L-D, Liu J, Yu X-F, He M, Pei X-F, Tang Z-Y, Wang QQ, Pang DW, Li Y. 2008 The biocompatibility of quantum dot probes used for the targeted imaging of hepatocellular carcinoma metastasis. *Biomaterials* **29**, 4170–4176. (doi:10.1016/j.biomaterials.2008.07.025)
88. Smith AM, Ruan G, Rhyner MN, Nie S. 2006 Engineering luminescent quantum dots for *in vivo* molecular and cellular imaging. *Ann. Biomed. Eng.* **34**, 3–14. (doi:10.1007/s10439-005-9000-9)
89. Miller K. 2002 Immunocytochemical techniques. In *Theory and practice of histological techniques*, 5th edn (eds J Bancroft, M Gamble), pp. 421–464. London, UK: Harcourt Publishers Limited.
90. Zheng Y, Wang XY, Wang YM, Liu XY, Zhang CM, Hou BX, Wang SL. 2012 Dentin regeneration using deciduous pulp stem/progenitor cells. *J. Dental Res.* **91**, 676–682. (doi:10.1177/0022034512449834)
91. Wessels JT, Yamauchi K, Hoffman RM, Wouters FS. 2010 Advances in cellular, subcellular, and nanoscale imaging *in vitro* and *in vivo*. *Cytometry A* **77**, 667–676. (doi:10.1002/cyto.a.20931)
92. Mierke CT *et al*. 2010 Vinculin facilitates cell invasion into three-dimensional collagen matrices. *J. Biol. Chem.* **285**, 13 121–13 130. (doi:10.1074/jbc.M109.087171)
93. Blackwood KA *et al*. 2008 Development of biodegradable electrospun scaffolds for dermal replacement. *Biomaterials* **29**, 3091–3104. (doi:10.1016/j.biomaterials.2008.03.037)
94. Liu X, Zhao M, Lu J, Ma J, Wei J, Wei S. 2012 Cell responses to two kinds of nanohydroxyapatite with different sizes and crystallinities. *Int. J. Nanomed.* **7**, 1239–1250. (doi:10.2147/IJN.S28098)
95. Madani SY, Tan A, Dwek M, Seifalian AM. 2012 Functionalization of single-walled carbon nanotubes and their binding to cancer cells. *Int. J. Nanomed.* **7**, 905–914.
96. McNally EA, Schwarcz HP, Botton GA, Arsenault AL. 2012 A model for the ultrastructure of bone based

on electron microscopy of ion-milled sections. *PLoS ONE* **7**, e29258. (doi:10.1371/journal.pone.0029258)

97. Orsini G, Ruggeri A, Mazzoni A, Nato F, Falconi M, Putignano A, Di Lenarda R, Nanci A, Breschi L. 2008 Immunohistochemical localization of dentin matrix protein 1 in human dentin. *Eur. J. Histochem.* **52**, 215–220.
98. Boncompagni S, Rossi AE, Micaroni M, Beznoussenko GV, Polishchuk RS, Dirksen RT, Protasi F. 2009 Mitochondria are linked to calcium stores in striated muscle by developmentally regulated tethering structures. *Mol. Biol. Cell* **20**, 1058–1067. (doi:10.1091/mbc.E08-07-0783)
99. Wu S *et al*. 2010 Electron tomography of cryofixed, isometrically contracting insect flight muscle reveals novel actin–myosin interactions. *PLoS ONE* **5**, e12643 (doi:10.1371/journal.pone.0012643)
100. Zipfel WR, Williams RM, Webb WW. 2003 Nonlinear magic: multiphoton microscopy in the biosciences. *Nat. Biotechnol.* **21**, 1369–1377. (doi:10.1038/nbt899)
101. Göppert-Mayer M. 1931 Über elementarakte mit zwei quantensprüngen. *Ann. Phys.* **9**, 273–295. (doi:10.1002/andp.19314010303)
102. Kaiser W, Garret C. 1961 Two-photon excitation in $CaF_2$: $Eu^{2+}$. *Phys. Rev. Lett.* **7**, 229–231. (doi:10.1103/PhysRevLett.7.229)
103. Denk W, Strickler J, Webb W. 1990 Two-photon laser scanning fluorescence microscopy. *Science* **248**, 73–76. (doi:10.1126/science.2321027)
104. Freund I, Deutsch M. 1986 Optical second-harmonic microscopy, crossed-beam summation, and small-angle scattering in rat-tail tendon. *Biophys. J.* **50**, 693–712. (doi:10.1016/S0006-3495(86)83510-X)
105. Duncan MD, Reintjes J, Manuccia TJ. 1982 Scanning coherent anti-Stokes Raman microscope. *Opt. Lett.* **7**, 350–352. (doi:10.1364/OL.7.000350)
106. Bewersdorf J, Pick R, Hell SW. 1998 Multifocal multiphoton microscopy. *Opt. Lett.* **23**, 655–657. (doi:10.1364/OL.23.000655)
107. Nielsen T, Fricke M, Hellweg D, Andresen P. 2001 High efficiency beam splitter for multifocal multiphoton microscopy. *J. Microscopy* **201**, 368–376. (doi:10.1046/j.1365-2818.2001.00852.x)
108. Zipfel WR, Williams RM, Christie R, Nikitin AY, Hyman BT, Webb WW. 2003 Live tissue intrinsic emission microscopy using multiphoton-excited native fluorescence and second harmonic generation. *Proc. Natl Acad. Sci. USA* **100**, 7075–7080. (doi:10.1073/pnas.0832308100)
109. Chen W-L, Huang C-H, Chiou L-L, Chen T-H, Huang Y-Y, Jiang C-C, Lee HS, Dong CY. 2010 Multiphoton imaging and quantitative analysis of collagen production by chondrogenic human mesenchymal stem cells cultured in chitosan scaffold. *Tissue Eng. C, Methods* **16**, 913–920. (doi:10.1089/ten.tec.2009.0596)
110. Dittmar R, Potier E, Zandvoort M, Van Ito K. 2012 Assessment of cell viability in three-dimensional scaffolds using cellular auto-fluorescence. *Tissue Eng.* **18**, 198–204. (doi:10.1089/ten.tec.2011.0334)
111. Murua A, Portero A, Orive G, Hernández RM, De Castro M, Pedraz JL. 2008 Cell microencapsulation technology: towards clinical application. *J. Control. Release* **132**, 76–83. (doi:10.1016/j.jconrel.2008.08.010)
112. Abbah S, Lu W, Chan D, Cheung K, Liu W, Zhao F, Li ZY, Leong JC, Luk KD. 2006 *In vitro* evaluation of alginate encapsulated adipose-tissue stromal cells for use as injectable bone graft substitute. *Biochem. Biophys. Res. Commun.* **347**, 185–191. (doi:10.1016/j.bbrc.2006.06.072)
113. Hunt NC, Grover LM. 2010 Cell encapsulation using biopolymer gels for regenerative medicine. *Biotechnol. Lett.* **32**, 733–742. (doi:10.1007/s10529-010-0221-0)
114. Nicodemus GD, Bryant SJ. 2008 Cell encapsulation in biodegradable hydrogels for tissue engineering applications. *Tissue Eng. B, Rev* **14**, 149–165. (doi:10.1089/ten.teb.2007.0332)
115. Rezwan K, Chen QZ, Blaker JJ, Boccaccini AR. 2006 Biodegradable and bioactive porous polymer/inorganic composite scaffolds for bone tissue engineering. *Biomaterials* **27**, 3413–3431. (doi:10.1016/j.biomaterials.2006.01.039)
116. Gorustovich A, Roether J, Boccaccini AR. 2010 Effect of bioactive glasses on angiogenesis: a review of *in vitro* and *in vivo* evidences. *Tissue Eng.* **16**, 199–207. (doi:10.1089/ten.teb.2009.0416)
117. Derby B. 2012 Printing and prototyping of tissues and scaffolds. *Science* **338**, 921–926. (doi:10.1126/science.1226340)
118. Fedorovich NE, De Wijn JR, Verbout AJ, Alblas J, Dhert WJA. 2008 Three-dimensional fiber deposition of cell-laden, viable, patterned constructs for bone tissue printing. *Tissue Eng.* **14**, 127–133. (doi:10.1089/ten.2007.0158)
119. Rice WL, Firdous S, Gupta S, Hunter M, Po CW, Wang Y, Kim HJ, Kaplan DL, Georgakoudi I. 2008 Non-invasive characterization of structure and morphology of silk fibroin biomaterials using non-linear microscopy. *Biomaterials* **29**, 2015–2024. (doi:10.1016/j.biomaterials.2007.12.049)
120. Pawlicki M, Collins HA, Denning RG, Anderson HL. 2009 Two-photon absorption and the design of two-photon dyes. *Angew. Chem. Int. Ed. Engl.* **48**, 3244–3266. (doi:10.1002/anie.200805257)
121. Xu C, Zipfel W, Shear JB, Williams RM, Webb WW. 1996 Multiphoton fluorescence excitation: new spectral windows for biological nonlinear microscopy. *Proc. Natl Acad. Sci. USA* **93**, 10 763–10 768. (doi:10.1073/pnas.93.20.10763)
122. Boerboom RA, Krahn KN, Megens RTA, Van Zandvoort MAMJ, Merkx M, Bouten CVC. 2007 High resolution imaging of collagen organisation and synthesis using a versatile collagen specific probe. *J. Struct. Biol.* **159**, 392–399. (doi:10.1016/j.jsb.2007.04.008)
123. Friedrich O *et al*. 2010 Microarchitecture is severely compromised but motor protein function is preserved in dystrophic *mdx* skeletal muscle. *Biophys. J.* **98**, 606–616. (doi:10.1016/j.bpj.2009.11.005)
124. Kajiwara H, Yamaza T, Yoshinari M, Goto T, Iyama S, Atsuta I, Kido MA, Tanaka T. 2005 The bisphosphonate pamidronate on the surface of titanium stimulates bone formation around tibial implants in rats. *Biomaterials* **26**, 581–587. (doi:10.1016/j.biomaterials.2004.02.072)
125. Rubbens MP, Driessen-Mol A, Boerboom RA, Koppert MMJ, Van Assen HC, TerHaar Romeny BM, Baaijens FPT, Bouten CVC. 2009 Quantification of the temporal evolution of collagen orientation in mechanically conditioned engineered cardiovascular tissues. *Ann. Biomed. Eng.* **37**, 1263–1272. (doi:10.1007/s10439-009-9698-x)
126. Chen B, Liu Q, Zhang Y, Xu L, Fang X. 2008 Transmembrane delivery of the cell-penetrating peptide conjugated semiconductor quantum dots. *Langmuir* **24**, 11 866–11 871. (doi:10.1021/la802048s)
127. Delehanty JB, Mattoussi H, Medintz IL. 2009 Delivering quantum dots into cells: strategies, progress and remaining issues. *Anal. Bioanal. Chem.* **393**, 1091–1105. (doi:10.1007/s00216-008-2410-4)
128. Jaiswal JK, Mattoussi H, Mauro JM, Simon SM. 2003 Long-term multiple color imaging of live cells using quantum dot bioconjugates. *Nat. Biotechnol.* **21**, 47–51. (doi:10.1038/nbt767)
129. Muller-Borer BJ, Collins MC, Gunst PR, Cascio WE, Kypson AP. 2007 Quantum dot labeling of mesenchymal stem cells. *J. Nanobiotechnol.* **5**, 9. (doi:10.1186/1477-3155-5-9)
130. Liu E, Treiser MD, Johnson PA, Patel P, Rege A, Kohn J, Moghe PV. 2007 Quantitative biorelevant profiling of material microstructure within 3D porous scaffolds via multiphoton fluorescence microscopy. *J. Biomed. Mater. Res. B* **82**, 284–297. (doi:10.1002/jbm.b.30732)
131. Hegen A, Blois A, Tiron CE, Hellesøy M, Micklem DR, Jacques EN, Akslen LA, Lorens JB. 2011 Efficient *in vivo* vascularization of tissue-engineering scaffolds. *J. Tissue Eng. Regen. Med.* **5**, 52–62. (doi:10.1002/term.336)
132. Dempsey WP, Fraser SE, Pantazis P. 2012 SHG nanoprobes: advancing harmonic imaging in biology. *BioEssays* **34**, 351–360. (doi:10.1002/bies.201100106)
133. Kleinman D. 1962 Nonlinear dielectric polarisation in optical media. *Phys. Rev.* **126**, 1977–1999. (doi:10.1103/PhysRev.126.1977)
134. Boyd G, Kleinman D. 1968 Parametric interaction of focused Gaussian light beams. *J. Appl. Phys.* **39**, 3597–3639. (doi:10.1063/1.1656831)
135. Chen X, Nadiarynkh O, Plotnikov S, Campagnola PJ. 2012 Second harmonic generation microscopy for quantitative analysis of collagen fibrillar structure. *Nat. Protocols* **7**, 654–669. (doi:10.1038/nprot.2012.009)
136. Niklason LE, Yeh AT, Calle EA, Bai Y, Valentín A, Humphrey JD. 2010 Enabling tools for engineering collagenous tissues integrating bioreactors, intravital imaging, and biomechanical modeling. *Proc. Natl Acad. Sci. USA* **107**, 3335–3339. (doi:10.1073/pnas.0907813106)
137. Raub CB, Suresh V, Krasieva T, Lyubovitsky J, Mih JD, Putnam AJ, Tromberg BJ, George SC. 2007 Noninvasive assessment of collagen gel microstructure and mechanics using multiphoton

microscopy. *Biophys. J.* **92**, 2212–2222. (doi:10.1529/biophysj.106.097998)

138. König K, Schenke-Layland K, Riemann I, Stock UA. 2005 Multiphoton autofluorescence imaging of intratissue elastic fibers. *Biomaterials* **26**, 495–500. (doi:10.1016/j.biomaterials.2004.02.059)
139. Lu K, Chen J, Zhuo S, Zheng L, Jiang X, Zhu X, Zhao J. 2009 Multiphoton laser scanning microscopy of localized scleroderma. *Skin Res. Technol.* **15**, 489–495. (doi:10.1111/j.1600-0846.2009.00395.x)
140. Thrasivoulou C, Virich G, Krenacs T, Korom I, Becker DL. 2011 Optical delineation of human malignant melanoma using second harmonic imaging of collagen. *Biomed. Opt. Express.* **2**, 1282–1295. (doi:10.1364/BOE.2.001282)
141. Brown E, McKee T, diTomaso E, Pluen A, Seed B, Boucher Y, Jain RK. 2003 Dynamic imaging of collagen and its modulation in tumors *in vivo* using second-harmonic generation. *Nat. Med.* **9**, 796–800. (doi:10.1038/nm879)
142. Tan H-Y *et al*. 2006 Multiphoton fluorescence and second harmonic generation imaging of the structural alterations in keratoconus *ex vivo*. *Invest. Ophthalmol. Vis. Sci.* **47**, 5251–5259. (doi:10.1167/iovs.06-0386)
143. Teng SW *et al*. 2007 Multiphoton fluorescence and second-harmonic generation microscopy for imaging structural alterations in corneal scar tissue in penetrating full-thickness wound. *Arch. Ophthalmol.* **125**, 977–978. (doi:10.1001/archopht.125.7.977)
144. Nucciotti V, Stringari C, Sacconi L, Vanzi F, Fusi L, Linari M, Piazzesi G, Lombardi V, Pavone FS. 2010 Probing myosin structural conformation *in vivo* by second-harmonic generation microscopy. *Proc. Natl Acad. Sci. USA* **107**, 7763–7768. (doi:10.1073/pnas.0914782107)
145. Olivier N *et al*. 2010 Cell lineage reconstruction of early zebrafish embryos using label-free nonlinear microscopy. *Science* **329**, 967–971. (doi:10.1126/science.1189428)
146. Campagnola PJ, Millard AC, Terasaki M, Hoppe PE, Malone CJ, Mohler WA. 2002 Three-dimensional high-resolution second-harmonic generation imaging of endogenous structural proteins in biological tissues. *Biophys. J.* **81**, 493–508. (doi:10.1016/S0006-3495(02)75414-3)
147. Schürmann S, Von Wegner F, Fink RHA, Friedrich O, Vogel M. 2010 Second harmonic generation microscopy probes different states of motor protein interaction in myofibrils. *Biophys. J.* **99**, 1842–1851. (doi:10.1016/j.bpj.2010.07.005)
148. Raub CB, Putnam AJ, Tromberg BJ, George SC. 2010 Predicting bulk mechanical properties of cellularized collagen gels using multiphoton microscopy. *Acta Biomater.* **6**, 4657–4665. (doi:10.1016/j.actbio.2010.07.004)
149. Lee P-F, Yeh AT, Bayless KJ. 2009 Nonlinear optical microscopy reveals invading endothelial cells anisotropically alter three-dimensional collagen matrices. *Exp. Cell Res.* **315**, 396–410. (doi:10.1016/j.yexcr.2008.10.040)
150. Yannas IV, Tzeranis DS, Harley BA, So PTC. 2010 Biologically active collagen-based scaffolds: advances in processing and characterization. *Phil. Trans. R. Soc. A* **368**, 2123–2139. (doi:10.1098/rsta.2010.0015)
151. Oliveira SM, Ringshia RA, Legeros RZ, Clark E, Yost MJ, Terracio L, Teixeria CC. 2010 An improved collagen scaffold for skeletal regeneration. *J. Biomed. Mater. Res.* **94**, 371–379.
152. Rodrigues SC, Salgado CL, Sahu A, Garcia MP, Fernandes MH, Monteiro FJ. 2012 Preparation and characterization of collagen-nanohydroxyapatite biocomposite scaffolds by cryogelation method for bone tissue engineering applications. *J. Biomed. Mater. Res.* **101**, 1–15. (doi:10.1002/jbm.a.34394)
153. Schoof H, Apel J, Heschel I, Rau G. 2001 Control of pore structure and size in freeze-dried collagen sponges. *J. Biomed. Mater. Res.* **58**, 352–357. (doi:10.1002/jbm.1028)
154. Nadiarnykh O, Lacomb RB, Campagnola PJ, Mohler WA. 2007 Coherent and incoherent SHG in fibrillar cellulose matrices. *Opt. Express.* **15**, 3348–3360. (doi:10.1364/OE.15.003348)
155. Deng Y, Lin X-S, Zheng Z, Deng J-G, Chen J-C, Ma H, Chen GQ. 2003 Poly(hydroxybutyrate-co-hydroxyhexanoate) promoted production of extracellular matrix of articular cartilage chondrocytes *in vitro*. *Biomaterials* **24**, 4273–4281. (doi:10.1016/S0142-9612(03)00367-3)
156. Hu J-J, Humphrey JD, Yeh AT. 2009 Characterization of engineered tissue development under biaxial stretch using nonlinear optical microscopy. *Tissue Eng.* **15**, 1553–1564. (doi:10.1089/ten.tea.2008.0287)
157. Maiti S. 1997 Measuring serotonin distribution in live cells with three-photon excitation. *Science* **275**, 530–532. (doi:10.1126/science.275.5299.530)
158. Evans CL, Potma EO, Puoris'haag M, Côté D, Lin CP, Xie XS. 2005 Chemical imaging of tissue *in vivo* with video-rate coherent anti-Stokes Raman scattering microscopy. *Proc. Natl Acad. Sci. USA* **102**, 16 807–16 812. (doi:10.1073/pnas.0508282102)
159. Brackmann C, Gabrielsson B, Svedberg F, Holmaang A, Sandberg A-S, Enejder A. 2010 Nonlinear microscopy of lipid storage and fibrosis in muscle and liver tissues of mice fed high-fat diets. *J. Biomed. Opt.* **15**, 066008. (doi:10.1117/1.3505024)
160. Conovaloff A, Wang H-W, Cheng J-X, Panitch A. 2009 Imaging growth of neurites in conditioned hydrogel by coherent anti-Stokes Raman scattering microscopy. *Organogenesis* **5**, 149–155. (doi:10.4161/org.5.4.10404)
161. Potma EO, Cheng J-X, Xie XS. 2011 Coherent Raman imaging techniques and biomedical applications. *J. Biomed. Opt.* **16**, 021101. (doi:10.1117/1.3558735)
162. Strachan CJ, Windbergs M, Offerhaus HL. 2011 Pharmaceutical applications of non-linear imaging. *Int. J. Pharm.* **417**, 163–172. (doi:10.1016/j.ijpharm.2010.12.017)
163. Yue S, Cárdenas-Mora JM, Chaboub LS, Lelièvre SA, Cheng J-X. 2012 Label-free analysis of breast tissue polarity by Raman imaging of lipid phase. *Biophys. J.* **102**, 1215–1223. (doi:10.1016/j.bpj.2012.01.023)
164. Cheng JX, Book LD, Xie XS. 2001 Polarization coherent anti-Stokes Raman scattering microscopy. *Opt. Lett.* **26**, 1341–1343. (doi:10.1364/OL.26.001341)
165. Müller M, Zumbusch A. 2007 Coherent anti-Stokes Raman scattering microscopy. *ChemPhysChem* **8**, 2156–2170. (doi:10.1002/cphc.200700202)
166. Chu S-W, Tai S-P, Ho C-L, Lin C-H, Sun C-K. 2005 High-resolution simultaneous three-photon fluorescence and third-harmonic-generation microscopy. *Microsc. Res. Tech.* **66**, 193–197. (doi:10.1002/jemt.20160)
167. Debarre D, Supatto W, Pena A-M, Fabre A, Tordjmann T, Combettes L, Schanne-Klein MC, Beaurepaire E. 2006 Imaging lipid bodies in cells and tissues using third-harmonic generation microscopy. *Nat. Methods* **3**, 47–53. (doi:10.1038/nmeth813)
168. Quentmeier S, Denicke S, Gericke K-H. 2009 Two-color two-photon fluorescence laser scanning microscopy. *J. Fluoresc.* **19**, 1037–1043. (doi:10.1007/s10895-009-0503-x)
169. Kaushalya SK, Desai R, Arumugam S, Ghosh H, Balaji J, Maiti S. 2008 Three-photon microscopy shows that somatic release can be a quantitatively significant component of serotonergic neurotransmission in the mammalian brain. *J. Neurosci. Res.* **86**, 3469–3480. (doi:10.1002/jnr.21794)